DAMAGE PHENOMENON IN HIGHLY FILLED ELASTOMERS

by

Birkan Tunç

B.S., Mechanical Engineering, Yıldız Technical University, 2006

M.S., Mechanical Engineering, Istanbul Technical University, 2008

Submitted to the Institute for Graduate Studies in
Science and Engineering in partial fulfillment of
the requirements for the degree of
Doctor of Philosophy

Graduate Program in Mechanical Engineering

Boğaziçi University

2017

ACKNOWLEDGEMENTS

I would like to thank my supervisor Assoc. Prof. Şebnem Özüpek for her guidance, patience and understanding throughout my thesis and my education in Boğaziçi University. Her unlimited support and encouragements allowed me to perform such a work. She will always inspire me by her professional perspective to teaching, academic vision and guidance.

I am also grateful to Dr. Evgeny Podnos for his support, advices, computational assistance and many useful and challenging discussions throughout various stages of the research period.

I would also like to express my gratitude to the members of my thesis advisory committee; Assoc. Prof. C. Can Aydıner, Assoc. Prof. Nuri Ersoy and Prof. Özgen Ü. Çolak Çakır for the useful discussions during the process. I also thank defence jury members Prof. Fazıl Önder Sönmez and Assoc. Prof. Güllü Kızıltaş Şendur.

I gratefully acknowledge the financial support of Boğaziçi University Research Fund (Grant Number 11642).

I also thank Roketsan A.Ş. for providing the test data.

Many thanks to my wife Burcu for her patience, support and love during many years of this research.

And finally, special thanks to my parents Aynur Tunç and Hüseyin Tunç who provided all the motivation during the research period and who make me feel their endless support during every minutes of my life.

ABSTRACT

DAMAGE PHENOMENON IN HIGHLY FILLED ELASTOMERS

The complete pathway to construct a constitutive model well suited for finite element analysis of highly filled elastomeric materials undergoing large deformation and damage was studied. The effects of viscoelasticity, temperature, superimposed pressure, cyclic loading and damage in the form of interface debonding were included in the model. Damage initiation and evolution criteria were defined, and the softening effect of damage on the stress response was modelled. A robust numerical algorithm was developed and implemented as a user material into a commercial finite element software. The model parameters were determined for a set of solid propellant test data. Using the calibrated constitutive model a systematic verification and validation procedure of the implementation was carried out. Homogeneous and inhomogeneous deformation states were considered and various element types were investigated. Model predictions at various loading rates, temperatures and superimposed pressure levels were compared to test data not used in the calibration. Three dimensional stress analysis of a solid rocket motor subjected to cyclic temperature loading was successfully completed. The constitutive model has good predictive capabilities for moderate loading rates, wide range of superimposed pressure levels and cyclic loading. At high loading rates and cold temperatures the model overpredicts the stress response. The implementation is stable and robust in terms of convergence. It is therefore concluded that the constitutive model can be readily used for stress analysis of highly filled elastomeric media with general geometry and loading.

ÖZET

YOĞUN DOLGULU ELASTOMERİK MALZEMELERDE HASAR OLGUSU

Çalışmada sonlu şekil değişimi ve hasara uğrayan yoğun dolgulu elastomer malzemeler için sonlu elemanlar analizine uyumlu bünye denklemi geliştirilmiştir. Viskoelastisite, sıcaklık, dış basınç, çevrimsel yükler ve tanecik-matris ara yüzeyindeki ayrılma sonucu oluşan hasarın etkileri modelde öngörülmektedir. Oluşan hasarın başlangıç ve gelişim kriteri belirlenmiş ve malzeme gerilmesinde hasar kaynaklı oluşan yumuşamalar modellenmiştir. Bünye denklemi, bir ticari sonlu elemanlar yazılımına kullanıcı tarafından tanımlanan malzeme modeli olarak entegre edilmiş ve bu amaçla sağlam bir sayısal algoritma geliştirilmiştir. Modelin parametreleri bir katı roket yakıtına ait deney verileri kullanılarak belirlenmiştir. Kalibrasyonu yapılan modelin sonlu elemanlar analizi uyarlamasına yönelik doğrulama ve gerçekleme çalışmaları yapılmıştır. Bu amaçla homojen ve homojen olmayan şekil değişimleri ve sonlu elemanlar analizinde kullanılan farklı eleman tipleri incelenmiştir. Değişik hız, sıcaklık ve dış basınçta yapılan ve kalibrasyonda kullanılmayan deney verileri ile model öngörüleri karşılaştırılmıştır. Katı yakıtlı roket motorunun çevrimsel sıcaklık yükleri altında üç boyutlu sonlu eleman analizleri başarı ile gerçekleştirilmiştir. Bünye modeli, ortalama hızlarda, tüm dış basınçlarda ve çevrimsel yüklemelerde deney verileri ile oldukça uyumlu sonuçlar vermektedir. Yüksek hızlarda ve düşük sıcaklıklardaki gerilme öngörüleri deney verilerinin üzerinde kalmaktadır. Önerilen sayısal algoritma ile modelin sonlu elemanlar yazılımına entegrasyonu sonucunda yakınsama sorunları ile karşılaşılmamıştır. Sonuç olarak, bu çalışmada geliştirilen bünye modeli yoğun dolgulu elastomer malzemelerden oluşan, herhangi bir geometriye sahip ve karmaşık yükler altındaki yapıların gerilme analizinde kullanılabilir.

TABLE OF CONTENTS

LIST OF FIGURES

LIST OF TABLES

LIST OF SYMBOLS

a_T	Time-temperature shift function
$\mathbf{C}, \bar{\mathbf{C}}$	Right Cauchy-Green strain tensor and its distortional part
c, c_{max}	Void content and its maximum value
c_1, c_2	Shift function parameters
c_{10}	Neo-Hookean energy density coefficient
$\mathbf{D}$	Rate of deformation tensor
DEV	$DEV(\bullet) = (\bullet) - \frac{1}{3}[\mathbf{C} : (\bullet)]\mathbf{C}^{-1}$
$\mathbf{E}, \bar{\mathbf{E}}$	Green strain and its distortional part
$\mathbf{F}$	Deformation gradient
$f(s_f)$	Cyclic loading function
f_u	Cyclic loading function during unloading
f_r	Cyclic loading function during reloading
G, K	Shear and bulk relaxation functions
G_0, K_0	Initial shear and bulk moduli
G_∞, K_∞	Equilibrium shear and bulk moduli
G_i, K_i	Prony coefficients of shear and bulk moduli
$g(s_g)$	Damage function
$\mathbf{H}, \mathbf{\Pi}$	Deviatoric part of viscoelastic and elastic stresses
I_1, I_2, I_3	Invariants of Right Cauchy-Green strain tensor
$\bar{I}_1, \bar{I}_2$	Invariants of deviatoric Right Cauchy-Green strain tensor
$I_{1,\sigma}, I_{2,\sigma}$	Invariants of Cauchy stress
$\bar{I}_{\gamma(t)}$	Distortional deformation
$\bar{I}_{\gamma max}$	Maximum value of distortional deformation
J	Volume change ratio
J_c	Volume change ratio due to inelastic deformations
J_e	Volume change ratio due to elastic deformations
J_{th}	Volume change ratio due to thermal effects
$\mathbf{L}$	Tangent stiffness

$\mathbf{L}^{vol}, \mathbf{L}^{dev}$	Volumetric and deviatoric parts of tangent stiffness
$P, \bar{P}$	Volumetric part of viscoelastic and elastic stresses
$\mathbf{P}$	First Piola-Kirchhoff stress
s_g, s_f	Internal state variables
$\mathbf{S}$	Viscoelastic second Piola-Kirchhoff stress
$\mathbf{S}_e$	Elastic second Piola-Kirchhoff stress
T, T_0	Temperature and its reference value
U^0	Volumetric part of strain energy density function
$\mathbf{W}$	Spin tensor
α_{th}	Thermal expansion coefficient
γ	Internal state variable
ϵ_i	Nominal strain
ϵ_L	Logaritmic strain
λ_i	Principal stretch ratios
ξ	Reduced time
$\boldsymbol{\sigma}$	Cauchy stress
σ_{shear}	Octahedral shear stress
σ_{crit}	Critical value of octahedral shear stress
τ_i	Characteristic times
ψ^0	Strain energy density function
$\bar{\psi}^0$	Deviatoric part of strain energy density function
$\omega_1, \omega_2, \omega_3, \omega_4, \omega_5, \omega_6$	Damage model parameters

LIST OF ACRONYMS/ABBREVIATIONS

DBST	Dual bond stress and temperature sensor
det	Determinant
ln	Natural logarithm
log	Logarithm with base 10
tr	Trace operator
UMAT	User defined material
WLF	Williams-Landel-Ferry equation

1. INTRODUCTION

1.1. Description of the problem

Composite solid propellants are lightly cross-linked polymers filled with high volume fraction of energetic constituents and were studied in this dissertation as an example of a highly filled elastomeric material. Their highly nonlinear mechanical behaviour due to large deformation and damage makes the constitutive modelling a challenging task. Temperature, loading rate, superimposed pressure, cyclic loading, particle-binder interface debonding are important factors that affect the mechanical response of solid propellants. Constitutive models that account for the effect of these factors may be mathematically quite complex and may need a large number of test data for calibration of model parameters. Solid propellant grain is typically placed in a steel or composite casing which has complex geometry and is exposed to different loading conditions such as pressure and inertia loads during launch and cyclic temperature loading during storage. Since the material response is highly temperature dependent, the service life of solid propellant is affected by the cyclic temperature loading. For accurate prediction of service life the determination of stress and strain field of the motor under cyclic thermal loading is essential. The complex geometry and loading of the motor requires three dimensional stress analyses, hence three dimensional implementation of the material model into finite element software.

Considering the complex mechanical behaviour and the need for three dimensional analysis, a constitutive model developed as part of a computational procedure, such as finite element analysis, needs to realistically predict the behaviour of the propellant under various loading conditions, be well suited for numerical implementation and preferably require moderate amount of test data to have extensive practical use in the industry. In addition, due to complexity of the mathematical model of the propellant, particular attention needs to be paid to the numerical stability and robustness of the algorithm to minimize convergence difficulties for complex deformation states.

1.2. Objectives

The objectives of this dissertation were to select a suitable basic constitutive model, enhance the model, develop a robust numerical algorithm, implement the algorithm into a commercial finite element code and perform stress analysis of a rocket motor that can be used to estimate service life of the solid propellant. Enhanced model aimed to realistically represent the solid propellant behaviour and use moderate amount of test data for calibration.

A basic constitutive model which is valid for any deformation range and has a suitable form to include damage effects was selected. The model was enhanced in terms of predictive capability of mechanical behaviour under various environmental and loading conditions. The effects of viscoelasticity, temperature, superimposed pressure, cyclic loading and damage in the form of interface debonding were included in the model. Damage initiation and evolution criteria were defined and the softening effect of damage on the stress response was modelled.

A stable numerical algorithm was developed. Particular attention was given to the implementation of the damage and cyclic softening functions to prevent convergence difficulties in three dimensional stress analysis. Commercial finite element code ABAQUS [1] was used for implementation of the model as a user material.

A systematic calibration, verification and validation procedure of the implementation of the constitutive model was developed. The particular real application considered in this dissertation was the stress analysis of a rocket motor under cyclic thermal loading for which predictions with damaging constitutive models are not available in the literature.

1.3. Literature Review

In the following, recent literature on propellant constitutive modelling is evaluated in terms of model development, computational implementation, verification-validation, and employment in stress analysis.

Simo [2] presented a three dimensional nonlinear viscoelastic damaging constitutive model which can be used in stress analysis. This work was pioneering in setting the computational framework for constitutive modelling of finitely deforming nearly incompressible materials.

Park and Schapery [3] presented a viscoelastic constitutive model with growing damage based on thermodynamics framework and internal state variables. The model is validated for uniaxial homogeneous deformations.

Jinseng *et al.* [4] proposed a thermo-damage viscoelastic constitutive model based on Park and Schapery [3] and presented step by step determination of the model parameters. The validation is based on uniaxial test data for homogeneous deformations.

Ha and Schapery [5] extended the model presented by Park and Schapery to three dimensions. Simulation results for biaxial specimen under different loading cases were presented. The model is valid only for small rotations.

Wang *et al.* [6] investigated the behaviour of propellants under low temperature and high strain rate employing a constitutive model of the type presented by Park and Schapery. The predictions agree well with the test data for uniaxial homogeneous deformations. The model is limited to small deformations and its extension to three dimensional analysis is not provided.

Xu *et al.* [7] accounted for porosity by including a model parameter in a linear viscoelastic constitutive model. The predictions for uniaxial monotonic and cyclic straining represented the test data for loading, however did not capture the nonlinear effects during unloading. The predictive capability for three dimensional analysis was not provided.

Han *et al.* [8] proposed a time-damage superposition method analogous to time-temperature superposition in order to account for mechanical ageing due to temperature cycle during storage. The model is based on linear viscoelasticity theory and its verification is presented for uniaxial test conditions.

Deng *et al.* [9] proposed a chemically aging linear viscoelastic constitutive model and its numerical algorithm as implemented in a finite element code. The response of a solid rocket motor grain for alternating temperature loading was presented.

Jung and Youn [10] presented a large strain viscoelastic constitutive model based on a viscoelastic dewetting criteria. This was an extension of the elastic dewetting criteria proposed by Vratsanos and Farris [11]. Based on this criteria critical stress for particle debonding was determined and the softening of the modulus, hence the softening in stress was calculated. The model compares well with test results for uniaxial straining at various strain rates and temperature. Calibration of the damaging model parameters such as adhesion energy and particle size distribution does not appear to be straightforward.

Jung *et al.* [12] proposed a computational algorithm for the viscoelastic constitutive model in [10] and they implemented it in ABAQUS software. Simulations of constant strain rate biaxial tests at various temperatures, constant strain rate uniaxial cyclic tests, and simultaneous straining-cooling tests agree reasonably well with data. Simulations for more complex geometries under general loading conditions are not provided.

Yun *et al.* [13] proposed an alternative damage function to [12] and provided the three dimensional computational algorithm for finite element implementation. The work presented in [12] and Yun *et al.* shows comparable results to test data for homogeneous stress states, however predictive capability of the constitutive model and the robustness of computational algorithm for a three dimensional geometry under loading conditions such as pressurization or cyclic temperature are not presented.

Chyuan [14] presented linear viscoelastic stress analysis of rocket motor to study the effect of thermal loading. In order to simulate the nonlinear response of the propellant he included into the constitutive model [15] the variation of bulk modulus with respect to compressive stresses. He showed that the effect of nonlinear bulk modulus on the response becomes important at temperatures higher than the stress-free temperature.

Hur *et al.* [16]'s constitutive model is based on the calculation of effective moduli of the propellant including the effect of void moduli, in addition to the binder and the particles. The moduli of the binder are assumed to depend on temperature and strain rate. Damage evolution is modelled as strain-controlled nucleation of voids. The model was implemented as user subroutine in a finite element code. The rate and temperature dependency of the matrix modulus improved the predictions under uniaxial straining at various rates and temperatures. Although the results were given for biaxial loading, the robustness of the algorithm under more complex loading states such as thermal cyclic loading were not published.

Huiru *et al.* [17] presented a three dimensional constitutive model for solid propellant considering time and temperature dependent Poisson's ratio. The model was implemented into commercial finite element code by using explicit integration scheme. The numerical results of three dimensional thermal cyclic and ignition pressurization analysis show that stress prediction with viscoelastic Poisson's ratio is much higher than the prediction with constant Poisson's ratio. The correspondence between elastic and viscoelastic Poisson's ratio is not clearly explained in the study. The model is valid for infinitesimal deformations only.

Guo *et al.* [18] presented the effect of liner properties on the stress and strain along liner-propellant interface. The results show that increased thermal expansion coefficient of the liner increases maximum principal stress along the rocket motor during cooling analysis. It is also shown that increased liner initial modulus increases the stress during cooling and ignition pressurization analysis while higher Poisson's ratio of liner decreases the stress during ignition pressurization analysis. The results can be used to determine suitable liner material to prevent interface debonding along the liner-propellant interface of the motor.

Liu *et al.* [19] presented test results for high performance propellant at various strain rates and temperatures. Based on dilatation measurements, it was concluded that for the initial linear portion of the deformation the material is almost incompressible while at higher strains volume change increases due to the formation of the voids following interface debonding. Experimental measurements seem to be more conclusive for dependence of initial slope of the stress-strain curve on strain rate and temperature. On the other hand, bulk modulus seems to have a complex dependence on strain rate and temperature.

Liu *et al.* [20] investigated the aging of HTPB propellant under thermo-mechanical loading. The propellant was aged under constant strain and temperature for various time durations. Maximum stress and strain values for each test were recorded and one dimensional aging model was calibrated. Acoustic emission and electron microscopy observations showed that thermal aging is dominant in the initial and final stages, while in the middle stages dewetting has the major contribution.

Bin *et al.* [21] presented a damaging viscoelastic model for the solid propellant. The definition of effective stress to represent damage was given. The constitutive model is based on linear viscoelasticity but it has the nonlinearity coming from the damage model. The model was implemented in a finite element code. The algorithm was validated with respect to analytical results for uniaxial creep loading. A three dimensional solid rocket motor model was built and the results were presented for internal pressurization.

In summary, although various damaging mechanical models for propellants are available in the literature, few of these follow with the implementation in a computational software and even fewer are concerned with the three dimensional finite element analyses. Most of the work in constitutive modelling of solid propellants is based mainly on the stress analysis of uniaxial or simple three dimensional models subjected to mechanical loadings which result in homogeneous deformations. Three dimensional nonlinear viscoelastic stress analysis of rocket motor having complex geometrical properties under cyclic thermal loading with damaging constitutive model is not presented in any of the researches published in the literature.

The particular basic finite strain viscoelastic model considered in this dissertation is based on Simo's framework [2]. The effect of damage is incorporated by adopting and enhancing the model presented by Özüpek and Becker [22]. A robust computational algorithm for the resulting damaging finite strain viscoelastic model is developed and implemented into commercial software ABAQUS.

Organization of the remainder of the dissertation is as follows:

The large deformation constitutive theory and the damage model are presented in Chapter 2.

The computational algorithm and the required set of equations are described in Chapter 3.

Chapter 4 is concerned with the model calibration along with the necessary tests to determine the model parameters.

Chapter 5 focuses on the verification of the undamaging user material subroutine for different loading conditions and various types of three dimensional elements. The implementation of the model without damage is verified against the built-in material model available in the software.

Damaging constitutive model validation is presented in Chapter 6. The predictive capability of the model with damage is validated against test data for various loading conditions.

The finite element model of rocket motor under cyclic temperature loading is described in Chapter 7. Stress analysis predictions are presented and comparison to the stress measured by dual bond stress and temperature sensor is given.

Summary, conclusions and discussions regarding future developments are presented in Chapter 8.

2. CONSTITUTIVE MODEL

The three dimensional nonlinear viscoelastic constitutive model described in this section represents the effects of strain rate, temperature, superimposed pressure and cyclic loading on the stress and dilatational response of the propellant. The basic finite strain model uses the framework of Simo. The damage model uses the dilatation model of Özüpek and Becker. Damage initiation and damage evolution criteria are proposed to account for the softening of the stress response. In this chapter, first, the fundamental quantities necessary for finite strain analysis are summarized. Following viscoelastic constitutive model and damage model are presented. Finally, softening during cyclic loading is addressed.

2.1. Basic Quantities in Large Deformation Analysis

The constitutive model and the numerical algorithm in this dissertation use Lagrangian framework of the large deformation theory. In this section a brief summary of fundamental quantities to be used in the remainder of the dissertation is given.

2.1.1. Kinematics

The fundamental quantity in finite deformation kinematics is the deformation gradient $\mathbf{F}$ which gives the relation of $d\mathbf{X}$, a material line in reference configuration, to $d\mathbf{x}$, the line in current configuration. The relation is given as

$$d\mathbf{x} = \mathbf{F}.d\mathbf{X} \tag{2.1}$$

Deformation gradient is given in explicit form as

$$\mathbf{F} = \frac{\partial \mathbf{x}}{\partial \mathbf{X}} = \begin{bmatrix} \frac{\partial x_1}{\partial X_1} & \frac{\partial x_1}{\partial X_2} & \frac{\partial x_1}{\partial X_3} \\ \frac{\partial x_2}{\partial X_1} & \frac{\partial x_2}{\partial X_2} & \frac{\partial x_2}{\partial X_3} \\ \frac{\partial x_3}{\partial X_1} & \frac{\partial x_3}{\partial X_2} & \frac{\partial x_3}{\partial X_3} \end{bmatrix} \tag{2.2}$$

Finite element software ABAQUS, the code selected for the implementation of the constitutive model, provides access only to deformation gradient $\mathbf{F}$ in nonlinear analysis. Thus, all of the quantities regarding deformation should be defined in terms deformation gradient in the user material subroutine.

Geometric changes in a continuous medium can be measured in a number of ways. In reference configuration the general deformation measure which is independent of both translation and rotation is defined as

$$\mathbf{C} = \mathbf{F}^T.\mathbf{F} \tag{2.3}$$

where $\mathbf{C}$ is called Right Cauchy-Green deformation tensor. Nonlinear isotropic elastic response of solids is derived from a strain energy density function which is defined in terms of invariants of $\mathbf{C}$

$$\begin{aligned} I_1 &= tr\mathbf{C} \\ I_2 &= \tfrac{1}{2}\left[(tr\mathbf{C})^2 - tr\mathbf{C}^2\right] \\ I_3 &= J^2 = det\mathbf{C} \end{aligned} \tag{2.4}$$

where J is the volume change ratio. Distortional part of $\mathbf{C}$ is defined as

$$\bar{\mathbf{C}} = J^{-2/3}\mathbf{C} \tag{2.5}$$

The invariants of volume preserving part of the deformation are defined as

$$\begin{aligned} \bar{I}_1 &= I_1/I_3^{1/3} \\ \bar{I}_2 &= I_2/I_3^{2/3} \end{aligned} \tag{2.6}$$

A strain measure often used in large deformation analysis is the Green strain defined as

$$\mathbf{E} = \frac{1}{2}(\mathbf{F}^T.\mathbf{F} - \mathbf{I}) = \frac{1}{2}(\mathbf{C} - \mathbf{I}) \tag{2.7}$$

where $\mathbf{I}$ is the identity tensor. Distortional part of $\mathbf{E}$ is defined as

$$\bar{\mathbf{E}} = \frac{1}{2}(\bar{\mathbf{C}} - \mathbf{I}) \tag{2.8}$$

This dissertation uses Lagrangian framework where Green strain $\mathbf{E}$ is conjugate of the second Piola-Kirchhoff stress $\mathbf{S}$. Therefore, all of the derivatives in the tangent stiffness are computed with respect to Green strain.

Another strain measure useful in presenting test data is called nominal or engineering strain and is defined in terms of principal stretch ratios λ_i as

$$\epsilon_i = \lambda_i - 1 \tag{2.9}$$

The test measurements and model predictions presented in this work are given in terms of engineering strains.

2.1.2. Stress Measures

In this section a summary of various forms of stresses used in this dissertation is given. In order to define the stress at a material point, we consider a small tetrahedral element as shown in Figure 2.1. The traction vector $\mathbf{t^n}$ is defined as

$$\mathbf{t^n} = \lim_{\Delta a \to 0} \frac{\Delta \mathbf{f}(\mathbf{n})}{\Delta a} \tag{2.10}$$

where $\Delta \mathbf{f}(\mathbf{n})$ is the force acting on a small oblique area Δa and $\mathbf{n}$ is the unit normal which denotes the orientation of the area Δa. Equilibrium of the tetrahedral element gives

$$\mathbf{t^n} = \mathbf{n}.\boldsymbol{\sigma} \tag{2.11}$$

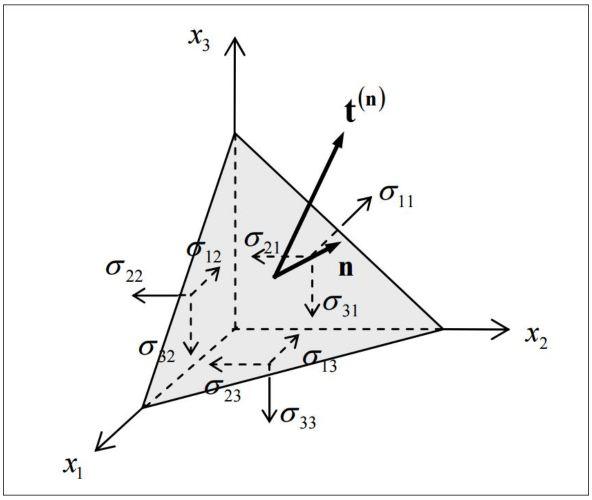

Figure 2.1. Tetrahedral element in cartesian coordinates.

which is known as the Cauchy stress formula and $\boldsymbol{\sigma}$ is the Cauchy stress defined as the force per unit deformed area. Since ABAQUS uses Eulerian frame work for the finite element analysis, the user material subroutine of the constitutive model developed in this dissertation needs to be expressed in terms of Cauchy stress.

Another measure of the stress is called the first Piola-Kirchhoff stress which is related to Cauchy stress $\boldsymbol{\sigma}$ as

$$\mathbf{P} = J\boldsymbol{\sigma}.\mathbf{F}^{-T} \tag{2.12}$$

The transpose of the first Piola-Kirchhoff stress is called nominal or engineering stress and it gives the current force per unit undeformed area. Uniaxial test measurements of solid propellant are given in terms of engineering stress which is obtained by dividing the force applied by the testing machine to undeformed cross-sectional area of the test specimen. The results and predictions regarding uniaxial tests in this dissertation are also given in terms of engineering stress. The first Piola-Kirchhoff stress is not commonly used in the finite element formulation since it is not symmetric, hence would result in time consuming computations during the simulations of models with large number of degrees of freedom.

A symmetric measure of stress is the second Piola-Kirchhoff stress which gives the transformed current force per unit undeformed area. It is related to Cauchy stress $\boldsymbol{\sigma}$ through

$$\mathbf{S} = J\mathbf{F}^{-1}.\boldsymbol{\sigma}.\mathbf{F}^{-T} \tag{2.13}$$

In this dissertation the constitutive model which is described in Section 2.2 is formulated in terms of the second Piola-Kirchhoff stress. This stress measure is widely used in the Lagrangian framework finite element analysis since the resulting tangent stiffness is also symmetric, hence computational effort is significantly reduced.

2.2. Viscoelastic Constitutive Model

The proposed three dimensional viscoelastic constitutive model is characterized by uncoupled deviatoric and volumetric responses. The separation of the response allows efficient formulation for nearly incompressible materials such as solid propellants and is suitable for the development of separate damage models for volumetric and deviatoric responses.

2.2.1. Elastic Response

Elastic response of the material model is derived from a strain energy density function which is expressed as an additive decomposition of volumetric and deviatoric parts as

$$\psi^0 = U^0(J) + g(s_g)\bar{\psi}^0(\bar{I}_1, \bar{I}_2) \tag{2.14}$$

where $g(s_g)$ accounts for the effect of damage on the distortional response as described in Section 2.3.1. The volumetric and deviatoric elastic stresses calculated from Equation 2.14 are, respectively

$$\bar{P} = \frac{\partial U^0}{\partial J} \qquad \text{and} \qquad \mathbf{\Pi} = g(s_g) J^{-2/3} DEV \left(\frac{\partial \bar{\psi}^0}{\partial \bar{\mathbf{E}}} \right) \tag{2.15}$$

Volumetric part of the strain energy function used in this study is of the form

$$U^0 = \frac{1}{2} K (J_e - 1)^2 \tag{2.16}$$

with

$$J_e = \frac{J}{J_{th} J_c}, \quad J_{th} = [1 + \alpha_{th}(T - T_0)]^3 \quad \text{and} \quad J_c = 1 + c(t) \tag{2.17}$$

where $c(t)$ is the void content as described in Section 2.3.

Distortional part of the elastic strain energy density is represented as the Neo-Hookean polynomial

$$\bar{\psi}^0 = c_{10}(\bar{I}_1 - 3) \tag{2.18}$$

where c_{10} is a material parameter. Elastic response of the material can be expressed in terms of second Piola-Kirchhoff stress as

$$\mathbf{S}_e = J \bar{P} \mathbf{C}^{-1} + f(s_f) \mathbf{\Pi} \tag{2.19}$$

Softening for unloading and reloading is represented by $f(s_f)$ as described in Section 2.3.2.

2.2.2. Viscoelasticity

Viscoelastic response is obtained by using integral formulation on the elastic stresses $\bar{P}$ and $\mathbf{\Pi}$.

$$P = \int_0^t \frac{K(\xi_t - \xi_\tau)}{K_0} \frac{\partial \bar{P}}{\partial \tau} d\tau \quad \text{and} \quad \mathbf{H} = \int_0^t \frac{G(\xi_t - \xi_\tau)}{G_0} \frac{\partial \mathbf{\Pi}}{\partial \tau} d\tau \tag{2.20}$$

where P and $\mathbf{H}$ are volumetric and deviatoric viscoelastic stresses, K_0 and G_0 are the initial bulk and shear moduli, respectively. ξ_t and ξ_τ are defined as

$$\xi_t = \xi(t) \quad \text{and} \quad \xi_\tau = \xi(\tau) \tag{2.21}$$

Viscoelastic second Piola-Kirchhoff stress is obtained by replacing elastic stresses in Equation 2.19 by the viscoelastic stresses in Equation 2.20 as

$$\mathbf{S}(t) = JP\mathbf{C}^{-1} + f(s_f)\mathbf{H} \tag{2.22}$$

Due to limitation of available test data, the propellant in this work is assumed to have thermorheologically simple behaviour. The change of shear and bulk moduli with temperature is taken into account by replacing the actual time t by the reduced time $\xi(t)$ as shown in Equation 2.20. The actual and reduced times are related to each other through the shift function a_T as

$$\xi(t) = \int_0^t \frac{d\eta}{a_T\left[T(\eta)\right]} \tag{2.23}$$

The shift function is a material property, typically determined from relaxation data at various temperatures. WLF equation is used in this dissertation to represent the shift function as

$$\log(a_T) = \frac{-c_1(T - T_0)}{c_2 + T - T_0} \tag{2.24}$$

where T and T_0 are the temperature and its reference value, c_1 and c_2 are material parameters.

2.3. Damage Model

Solid propellants subjected to loading exhibit dewetting, that is separation of particles from the binder followed by the formation of voids at the binder-particle interface. This phenomenon is macroscopically observed as volume increase, in an otherwise incompressible material. Experimental data showed that the volume change occurs under purely distortional deformation and its rate decreased with superimposed pressure.

In the damage model, the volume change resulting from formation of voids is represented with variable $c(t)$ which evolves according to

$$\dot{c}(t) = \dot{\gamma}(t) e^{P/\omega_1} \quad \text{and} \quad \dot{\gamma}(t) = \omega_2 \bar{I}_\gamma^{\omega_3}(t) \tag{2.25}$$

In Equation 2.25, $\gamma(t)$ accounts for the effect of distortional deformation, while exponential term represents the superimposed pressure effect, and ω_1, ω_2 and ω_3 are material parameters. Octahedral shear strain $\bar{I}_\gamma$ can be written in terms of volume preserving invariants as

$$\bar{I}_\gamma = \frac{1}{6} \left(2\bar{I}_1^2 - 6\bar{I}_2 \right)^{1/2} \tag{2.26}$$

The effect of voids on the volumetric response is captured by softening the initial bulk modulus according to

$$K = \frac{K_0}{1 + \omega_4 K_0 c(t)} \left[1 - c(t) \right] \tag{2.27}$$

where ω_4 is a material parameter to be determined.

2.3.1. Damage Initiation and Evolution

Solid propellants subjected to monotonic uniaxial or biaxial loading at a constant strain rate show softening of stress upon initiation of dewetting. It is assumed that dewetting, hence softening, starts when the octahedral shear stress reaches a critical value [13]. Octahedral shear stress is defined in terms of Cauchy stress invariants $I_{1,\sigma}$ and $I_{2,\sigma}$ as

$$\sigma_{shear} = \frac{1}{3}\sqrt{2I_{1,\sigma}^2 - 6I_{2,\sigma}} > \sigma_{crit} \tag{2.28}$$

The stress softening is represented with the function $g(s_g)$ introduced in Equation 2.14. Since initiation of dewetting leads to volume increase and is irreversible, the internal state variable s_g is considered to be the maximum value of void content reached throughout the loading history, that is

$$s_g = c_{max} \tag{2.29}$$

The rate of change of the function $g(s_g)$ with respect to s_g is proposed as

$$\dot{g}(s_g) = \frac{\mathrm{d}g(s_g)}{\mathrm{d}s_g} = \omega_5 \ln(s_g) e^{s_g/\omega_6} \tag{2.30}$$

where ω_5 and ω_6 are material parameters.

Since c_{max} cannot decrease during loading, $\dot{g}(s_g)$ is always positive. Thus, the softening effect resulting from $g(s_g)$ is permanent. The introduction of damage initiation and evolution model improved the predictive capability of the model at low temperatures and for biaxial tests as well as for the loading at transient temperature. The fact that damage evolution model has only two parameters to be determined allowed efficient implementation of the model in comparison to specifying the function $g(s_g)$ itself. The rate form also improved the convergence of the implementation during three dimensional stress analysis.

2.3.2. Softening for Unloading and Reloading

Solid propellants subjected to cyclic uniaxial or biaxial loading at a constant strain rate showed softening of stress during unloading and reloading. The cyclic hysteresis was greater than what viscoelasticity can account for. In the constitutive model described in this work the cyclic softening is represented with the function $f(s_f)$ which modifies the viscoelastic deviatoric stress as shown in Equation 2.22. The argument of $f(s_f)$ is defined as the ratio of the current octahedral shear strain to its maximum value within a cycle as

$$s_f = \frac{\bar{I}_\gamma}{\bar{I}_{\gamma_{max}}} \tag{2.31}$$

The cyclic function proposed here has three distinct branches for loading, unloading and reloading as

$$f = \begin{cases} 1, & \text{loading} \\ f_u, & \text{unloading} \\ f_r, & \text{reloading and unloading from reloading} \end{cases} \tag{2.32}$$

The cyclic function proposed in Equations 2.31 and 2.32 is a simplified version of the model introduced in a previous work [23]. The form given here resulted in an improved numerical performance and faster convergence with the same accuracy in the model's predictive capability for cyclic loading. In addition, oscillations in stress during transition from unloading to reloading in three dimensional stress analysis were eliminated. Finally, elimination of the additional terms of the previously suggested cyclic function simplified the implementation of the model into the finite element formulation.

3. COMPUTATIONAL ALGORITHM

In order to perform three dimensional finite element analysis, the constitutive model presented in Chapter 2 was implemented into commercial software ABAQUS as a user material subroutine UMAT for implicit simulation.

3.1. Stress Calculation

Upon substitution of Equation 2.20 into Equation 2.22, the viscoelastic constitutive model becomes

$$\mathbf{S}(t) = J\mathbf{C}^{-1}\int_0^t \frac{K(\xi_t-\xi_\tau)}{K_0}\frac{\partial \bar{P}}{\partial \tau}d\tau + f(s_f)\int_0^t \frac{G(\xi_t-\xi_\tau)}{G_0}\frac{\partial \mathbf{\Pi}}{\partial \tau}d\tau \tag{3.1}$$

Shear and bulk relaxation functions were expressed in Prony series form

$$G(t) = G_\infty + \sum_{i=1}^{m} G_i e^{-t/\tau_i} \quad \text{and} \quad K(t) = K_\infty + \sum_{i=1}^{m} K_i e^{-t/\tau_i} \tag{3.2}$$

Upon substitution of Prony series into Equation 3.1 we obtain

$$\begin{aligned}\mathbf{S}(t) = J\mathbf{C}^{-1}&\left[\bar{K}_\infty \bar{P} + \sum_{i=1}^{n}\bar{K}_i\int_0^t e^{(\xi_\tau-\xi_t)/\tau_i}\frac{\partial \bar{P}}{\partial \tau}d\tau\right]\\ +f(s_f)&\left[\bar{G}_\infty \mathbf{\Pi} + \sum_{i=1}^{n}\bar{G}_i\int_0^t e^{(\xi_\tau-\xi_t)/\tau_i}\frac{\partial \mathbf{\Pi}}{\partial \tau}d\tau\right]\end{aligned} \tag{3.3}$$

where the normalized moduli are

$$\bar{K}_\infty = \frac{K_\infty}{K_0}, \quad \bar{K}_i = \frac{K_i}{K_0}, \quad \bar{G}_\infty = \frac{G_\infty}{G_0}, \quad \bar{G}_i = \frac{G_i}{G_0} \tag{3.4}$$

The viscoelastic stress in Equation 3.3 needs to be integrated at each time step. Expressing time t with $n+1$ and assuming that elastic stresses vary linearly within time increment Δt, we obtain

$$\mathbf{S}_{n+1} = J\mathbf{C}^{-1}\left[\bar{K}_\infty \bar{P}_{n+1} + \sum_{i=1}^{m} \bar{K}_i \left[e^{-\Delta\xi/\tau_i}\bar{P}_n^i + \frac{1}{\Delta\xi}(\bar{P}_{n+1} - \bar{P}_n)\int_n^t e^{(\xi_\tau - \xi_t)/\tau_i} d\tau\right]\right] + f(s_f)\left[\bar{G}_\infty \mathbf{\Pi}_{n+1} + \sum_{i=1}^{m} \bar{G}_i \left[e^{-\Delta\xi/\tau_i}\mathbf{H}_n^i + \frac{1}{\Delta\xi}(\mathbf{\Pi}_{n+1} - \mathbf{\Pi}_n)\int_n^t e^{(\xi_\tau - \xi_t)/\tau_i} d\tau\right]\right] \tag{3.5}$$

where $\Delta\xi = \xi_t - \xi_\tau$. Integrating the exponential term analytically as

$$\int_n^t e^{(\xi_\tau - \xi_t)/\tau_i} d\tau = \tau_i(1 - e^{-\Delta\xi/\tau_i}) \tag{3.6}$$

and substituting the resulting Equation 3.6 into Equation 3.5 we can express the second Piola-Kirchhoff stress in compact form as

$$\mathbf{S}_{n+1} = J\mathbf{C}^{-1} P_{n+1} + f(s_f)\mathbf{H}_{n+1} \tag{3.7}$$

where

$$P_{n+1} = \bar{K}_\infty \bar{P}_{n+1} + \sum_{i=1}^{m} \bar{K}_i \bar{P}_{n+1}^i \tag{3.8}$$

$$\mathbf{H}_{n+1} = \bar{G}_\infty \mathbf{\Pi}_{n+1} + \sum_{i=1}^{m} \bar{G}_i \bar{\mathbf{H}}_{n+1}^i \tag{3.9}$$

The following history variables

$$\bar{P}_{n+1}^i = e^{-\Delta\xi/\tau_i}\bar{P}_n^i + \frac{\tau_i\left(1 - e^{-\Delta\xi/\tau_i}\right)}{\Delta\xi}\left(\bar{P}_{n+1} - \bar{P}_n\right) \tag{3.10}$$

$$\bar{\mathbf{H}}_{n+1}^i = e^{-\Delta\xi/\tau_i}\bar{\mathbf{H}}_n^i + \frac{\tau_i\left(1 - e^{-\Delta\xi/\tau_i}\right)}{\Delta\xi}\left(\mathbf{\Pi}_{n+1} - \mathbf{\Pi}_n\right) \tag{3.11}$$

are stored to be used in the next time increment.

Since the finite strain formulation of ABAQUS is expressed in terms of Cauchy stress, Equation 3.7 needs to be transformed to Cauchy stress using

$$\boldsymbol{\sigma} = \frac{1}{J}\mathbf{F}.\mathbf{S}.\mathbf{F}^T \tag{3.12}$$

3.2. Tangent Stiffness Calculation

For an implicit solver tangent stiffness needs to be provided. In particular ABAQUS requires Cauchy stress increment in the form

$$d\boldsymbol{\sigma}_{n+1} = d\mathbf{W}\boldsymbol{\sigma}_{n+1} + \boldsymbol{\sigma}_{n+1}d\mathbf{W}^T + \mathbf{L}^J d\mathbf{D} \tag{3.13}$$

where $\mathbf{D}$ is the rate of deformation tensor. Considering that ABAQUS uses Jaumann rate for solid elements, the tangent stiffness $\mathbf{L}^J$ is given as

$$L^J_{ijkl} = \wp_{ijkl} + \delta_{ik}\sigma_{jl} + \sigma_{jl}\delta_{ik}, \quad \wp_{ijkl} = \frac{1}{J}F_{ip}F_{jq}F_{kr}F_{ls}L_{pqrs} \quad \text{and} \quad L_{ijkl} = \frac{\partial S_{ij}}{\partial E_{kl}} \tag{3.14}$$

The Lagrangian tangent stiffness $\mathbf{L}$ can be expressed in terms of volumetric and deviatoric components as

$$\mathbf{L} = \frac{\partial \mathbf{S}}{\partial \mathbf{E}} = \mathbf{L}^{vol} + \mathbf{L}^{dev} \tag{3.15}$$

The volumetric and deviatoric parts of the Lagrangian tangent stiffness corresponding to the constitutive form given in Equation 3.1, are given as

$$\mathbf{L}^{vol} = \frac{\partial\left(J\mathbf{C}^{-1}P\right)}{\partial \mathbf{E}} = \left(\alpha J^2\frac{\partial^2 U^0}{\partial J^2} + JP\right)\mathbf{C}^{-1}\otimes\mathbf{C}^{-1} - 2JP\mathbf{I}_{C^{-1}} \tag{3.16}$$

and

$$
\begin{aligned}
\mathbf{L}^{dev} &= f(s_f)\frac{\partial \mathbf{H}}{\partial \mathbf{E}} \\
= g(s_g)f(s_f)J^{-2/3}\beta\Bigg\{ &-\frac{2}{3}\left[\frac{\partial\bar{\psi}^0}{\partial\bar{\mathbf{E}}}\otimes\mathbf{C}^{-1} - \frac{1}{3}\left(\frac{\partial\bar{\psi}^0}{\partial\bar{\mathbf{E}}}:\mathbf{C}\right)\mathbf{C}^{-1}\otimes\mathbf{C}^{-1}\right] \\
+J^{-\frac{2}{3}}\Bigg[\frac{\partial^2\bar{\psi}^0}{\partial\bar{\mathbf{E}}^2} - \frac{1}{3}\left(\frac{\partial^2\bar{\psi}^0}{\partial\bar{\mathbf{E}}^2}:\mathbf{C}\right)\otimes\mathbf{C}^{-1} &- \frac{1}{3}\mathbf{C}^{-1}\otimes\left(\frac{\partial^2\bar{\psi}^0}{\partial\bar{\mathbf{E}}^2}:\mathbf{C}\right) \\
+\frac{1}{9}\left(\mathbf{C}:\frac{\partial^2\bar{\psi}^0}{\partial\bar{\mathbf{E}}^2}:\mathbf{C}\right)\mathbf{C}^{-1}\otimes\mathbf{C}^{-1}\Bigg] - \frac{2}{3}\mathbf{C}^{-1}\otimes\frac{\partial\bar{\psi}^0}{\partial\bar{\mathbf{E}}} &+ \frac{2}{3}\left(\frac{\partial\bar{\psi}^0}{\partial\bar{\mathbf{E}}}:\mathbf{C}\right)\mathbf{I}_{C^{-1}}\Bigg\}
\end{aligned}
\tag{3.17}
$$

where

$$
\alpha = \bar{K}_\infty + \sum_{i=1}^{m}\bar{K}_i\frac{\tau_i\left(1-e^{-\Delta\xi/\tau_i}\right)}{\Delta\xi} \quad \text{and} \quad \beta = \bar{G}_\infty + \sum_{i=1}^{m}\bar{G}_i\frac{\tau_i\left(1-e^{-\Delta\xi/\tau_i}\right)}{\Delta\xi} \tag{3.18}
$$

and

$$
\left(I_{C^{-1}}\right)_{ijkl} = C^{-1}_{ik}C^{-1}_{jl} \tag{3.19}
$$

To improve the convergence of the numerical algorithm, $f(s_f)$ is set to its value at the previous time step. The softening function $g(s_g)$ is calculated in the algorithm during time increment Δt.

3.3. Shift Function

Time integration of above equations requires determination of reduced time increment $\Delta\xi$ in terms of actual time increment Δt. Since a_T varies nonlinearly with time, direct approximation of a_T yields large errors [1]. On the other hand $\log(a_T)$ is typically a smooth varying function of temperature, therefore it can be approximated by a linear function of temperature during time increment Δt, as

$$
-\log(a_T[T(t)]) = h(T) = a + bt \tag{3.20}
$$

or

$$a_T^{-1}[T(t)] = 10^{a+bt} \tag{3.21}$$

where

$$a = \frac{1}{\Delta t}\left[t^{n+1}h(T_n) - t^n h(T_{n+1})\right] \tag{3.22}$$

and

$$b = \frac{1}{\Delta t}\left[h(T_{n+1}) - h(T_n)\right] \tag{3.23}$$

Substituting Equation 3.22 and Equation 3.23 into Equation 2.23 we obtain

$$\begin{aligned}\Delta\xi &= \int_{t^n}^{t^{n+1}} 10^{a+bt}dt \\ &= \frac{1}{b\ln(10)}\left(10^{a+bt^{n+1}} - 10^{a+bt^n}\right)\end{aligned} \tag{3.24}$$

If the temperature T is constant during any time increment, the reduced time becomes

$$\Delta\xi = 10^{c_1(T_n - T_0)/(c_2+T_n-T_0)}\Delta t \tag{3.25}$$

3.4. Damage Model Variables

Evolution of the variables in Equations 2.25 are calculated in the algorithm as

$$\Delta\gamma(t) = \omega_2\left[\bar{I}_\gamma^{\omega_3}(t) - \bar{I}_\gamma^{\omega_3}(t-\Delta t)\right] \quad \text{and} \quad c(t) = c(t-\Delta t) + \Delta\gamma(t)e^{P(t-\Delta t)\omega_1} \tag{3.26}$$

Since the bulk modulus changes as a function of void content, the new value of the bulk modulus in a given iteration is calculated according to Equation 2.27 and volumetric part of elastic stress in Equation 2.15 is updated according to the new bulk modulus.

The current value of the softening function $g(s_g)$ in Equation 2.30 is calculated from

$$g(s_g)_t = g(s_g)_{t-\Delta t} + \dot{g}(s_g)_t \Delta s_g \tag{3.27}$$

Deviatoric part of elastic stress in Equation 2.15 is updated according to the current value of softening function.

The flow chart for user defined material model algorithm is given in Figure 3.1.

The computational algorithm for the nondamaging finite strain viscoelastic constitutive model can easily be obtained by setting $g(s_g) = 1$ and $f(s_f) = 1$ in Equation 2.15 and in Equation 2.22, $c(t) = 0$ in Equation 2.25 and $K = K_0$ in Equation 2.27 during computation. The flow chart corresponding to nondamaging model is shown in Figure 3.1.

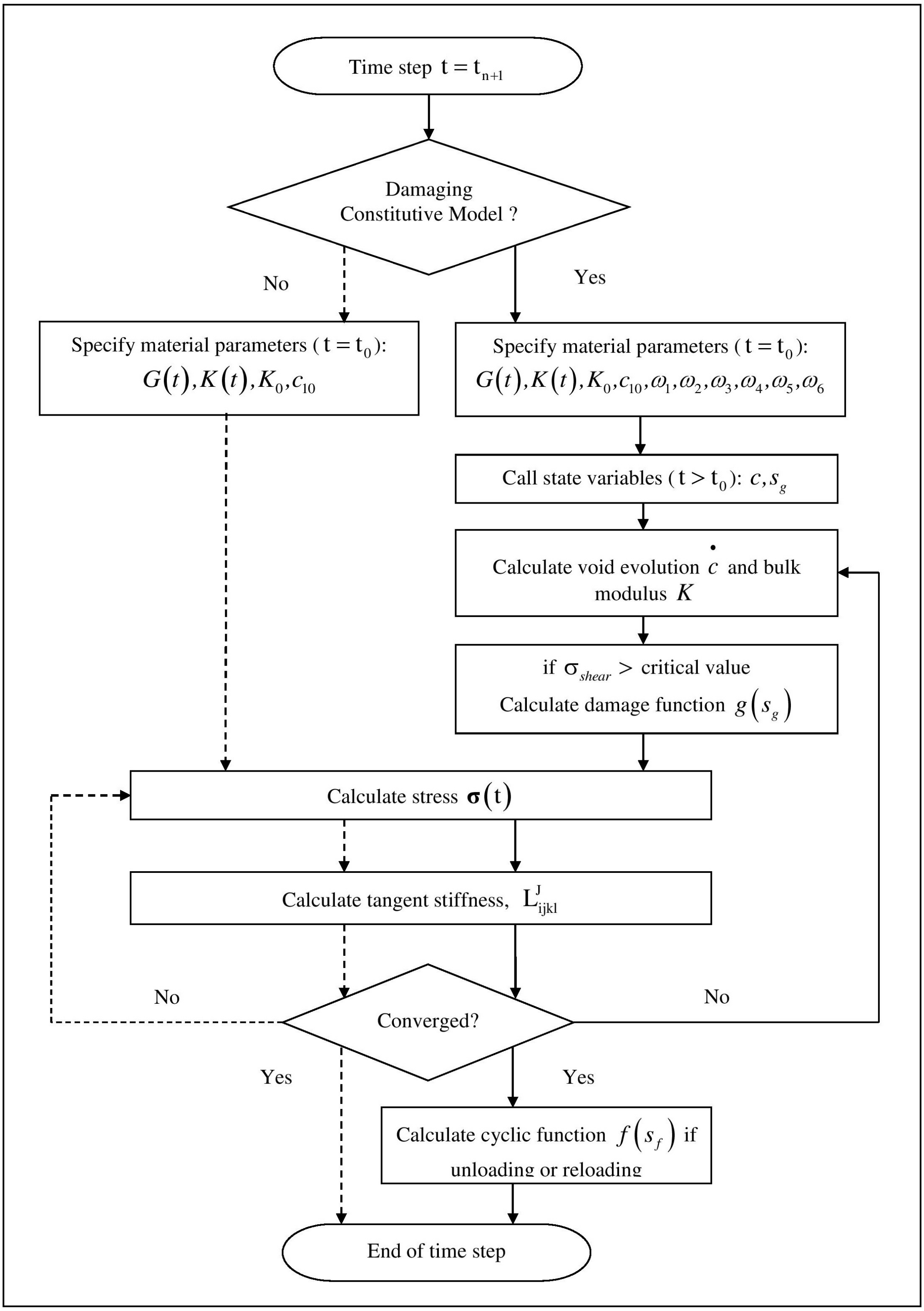

Figure 3.1. Flow chart of the algorithm for user defined material model.

4. CONSTITUTIVE MODEL CALIBRATION

In this section, the calibration of the constitutive model, that is the determination of shear and bulk relaxation, strain energy, damage and unloading-reloading functions, is described. The list of materials parameters to be determined is shown in Table 4.1.

Table 4.1. Material parameters of the constitutive model.

Prony Terms	WLF	Hyperelastic Coefficients	Damage Model Parameters
G_i	T_0	c_{10}	ω_1, ω_2
G_∞	c_1	K_0	ω_3, ω_4
τ_i	c_2		ω_5, ω_6
			σ_{crit}

4.1. Relaxation Functions

Shear and bulk relaxation of the material were assumed to be the same. Tensile relaxation test data at various temperatures, as shown in Figure 6.1, were used to determine the time-temperature equivalence, i.e. the shift function, and to construct the master curve. The reference temperature was selected as 20 $°C$. The master curve was represented as Prony series:

$$G(t) = G_\infty + \sum_{i=1}^{m} G_i e^{-t/\tau_i} \quad \text{and} \quad K(t) = K_\infty + \sum_{i=1}^{m} K_i e^{-t/\tau_i} \tag{4.1}$$

In particular, characteristic times τ_i were selected one decade apart and the coefficients G_i were calculated using least-squares technique. The shift function was represented in WLF form. The constants c_1 and c_2 in Equation 2.24 were determined from a least-square curve fit to shift data.

4.2. Energy Function

Stress-strain data from a uniaxial constant strain rate test at 0.724 min^{-1} and 20 $^{\mathrm{o}}C$, Figure 6.2, were used to determine the energy function. A Neo-Hookean form was selected and test data up to the beginning of stress softening were used to determine the coefficient c_{10} of Equation 2.18. Damage function $g(s_g)$ and cyclic function $f(s_f)$ were set to unity.

The following numerical algorithm was developed to perform the calibration. Following the definitions provided in Chapter 3, second Piola-Kirchhoff stress in the loading direction of a homogeneous uniaxial deformation can be written as

$$\begin{aligned} S_{11,n+1} = JC_{11}^{-1} &\left[\bar{K}_\infty \bar{P}_{n+1} + \sum_{i=1}^{m} \bar{K}_i \bar{P}_{n+1}^i \right] \\ +f(s_f) &\left[\bar{G}_\infty \Pi_{11,n+1} + \sum_{i=1}^{m} \bar{G}_i \bar{H}_{11,n+1}^i \right] \end{aligned} \tag{4.2}$$

where

$$\bar{P}_{n+1}^i = e^{-\Delta\xi/\tau_i} \bar{P}_n^i + \frac{\tau_i(1 - e^{-\Delta\xi/\tau_i})}{\Delta\xi} (\bar{P}_{n+1} - \bar{P}_n) \tag{4.3}$$

and

$$H_{11,n+1}^i = e^{-\Delta\xi/\tau_i} H_{11,n}^i + \frac{\tau_i(1 - e^{-\Delta\xi/\tau_i})}{\Delta\xi} (\Pi_{11,n+1} - \Pi_{11,n}) \tag{4.4}$$

are stored as history variables to be used in the next time increment. Elastic part of deviatoric stress containing damage function $g(s_g)$ can be written explicitly as

$$\Pi_{11} = g(s_g) J^{-2/3} DEV \left(\frac{\partial \bar{\psi}^0}{\partial \bar{\mathbf{E}}} \right)_{11} \tag{4.5}$$

Stress components in the transverse directions to the uniaxial loading can be expressed as

$$
\begin{aligned}
S_{22,n+1} = S_{33,n+1} = JC_{22}^{-1} & \left[\bar{K}_{\infty} \bar{P}_{n+1} + \sum_{i=1}^{m} \bar{K}_i \bar{P}^i_{n+1} \right] \\
+ f(s_f) & \left[\bar{G}_{\infty} \Pi_{22,n+1} + \sum_{i=1}^{m} \bar{G}_i \bar{H}^i_{22,n+1} \right]
\end{aligned}
\tag{4.6}
$$

Right Cauchy-Green deformation tensor is expressed in terms of principal stretches λ_i as

$$
\mathbf{C} = \sum_{i=1}^{3} \lambda_i^2 \mathbf{N}_i \otimes \mathbf{N}_i \tag{4.7}
$$

where $\mathbf{N}_i$ are the principal directions.

Expressing Equation 4.7 for homogeneous uniaxial deformation for which $\lambda_3 = \lambda_2$ Equation 4.2 and Equation 4.6 can be written in terms of the principal stretches λ_1 and λ_2. For a given uniaxial loading history, that is for known values of λ_1, λ_2 can be solved fom $S_{22}(t) = 0$ by Newton-Raphson as

$$
\lambda_2 \Big|_{i+1} = \lambda_2 \Big|_{i} + \left[S_{22}(t) / \frac{dS_{22}(t)}{d\lambda_2} \right] \Bigg|_{i+1} \tag{4.8}
$$

Once λ_2 is found, $S_{11}(t)$ is calculated from Equation 4.2 where the volume change ratio is

$$
J = \lambda_1 \lambda_2^2 \tag{4.9}
$$

The Neo-Hookean coefficient c_{10} which is part of Equation 4.5

$$
\frac{\partial \bar{\psi}^0}{\partial \bar{\mathbf{E}}} = 2 \frac{\partial \bar{\psi}^0}{\partial \bar{\mathbf{C}}} = 2 \frac{\partial \bar{\psi}^0}{\partial \bar{I}_1} \frac{\partial \bar{I}_1}{\partial \bar{\mathbf{C}}} = 2 c_{10} \mathbf{I} \tag{4.10}
$$

is calibrated using the least-squares technique.

The value of the initial bulk modulus is not critical as long as it is selected such that the material behaves incompressible before the onset of damage. In this work K_0 was selected approximately as 10^4 times the initial shear modulus.

Thermal expansion coefficient was measured through the standard test methods.

4.3. Damage Functions

The damage model presented in Section 2.3 requires the determination of dilatation parameters ω_1, ω_2, ω_3 in Equation 2.25, bulk material parameter ω_4 in Equation 2.27 and stress softening parameters ω_5, ω_6 in Equation 2.30. Stress-dilatation-strain data of uniaxial constant strain rate test at 0.724 min^{-1} and 20 $°C$, Figure 6.2, were used for determining all ω_i values as detailed in the following.

The first step in calibration process of damage model consisted of determination of dilatational parameters. At this point the softening functions $g(s_g)$ and $f(s_f)$ were set to unity and an initial guess was made for ω_1, ω_2, ω_3 and ω_4. The least-squares technique was used until a good fit to test data was obtained for S_{11} in Equation 4.2 and J in Equation 4.9.

The second step consisted of finding stress softening parameters ω_5, ω_6 and σ_{crit}. At this stage only $f(s_f)$ was set to unity. Dilatational parameters obtained in Step 1 were used. An initial guess was made for ω_5, ω_6 and σ_{crit} and Equation 4.2 was solved for softening parameters. σ_{crit} was found almost equal to octahedral shear stress at which the prediction of nondamaging model started to deviate from the test data.

Following Step 2, that is once softening parameters were determined, Step 1 and Step 2 were repeated until a good fit was obtained for both dilatational and stress softening parameters. The procedure took a few iterations to obtain a good fit. Flowchart of the calibration procedure is shown in Figure 4.1. The softening function resulting from the calibration is shown in Figure 4.2.

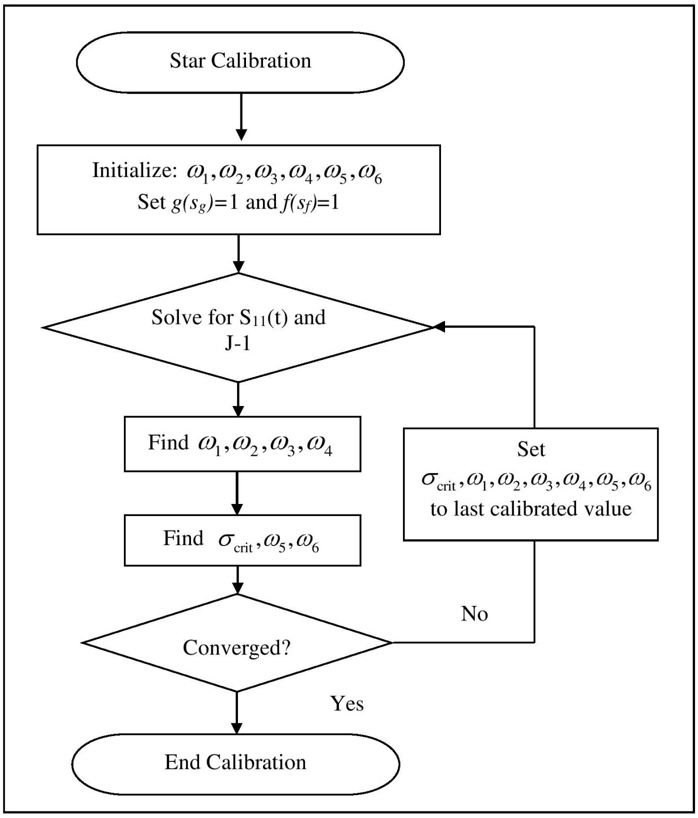

Figure 4.1. Flow chart of the calibration procedure.

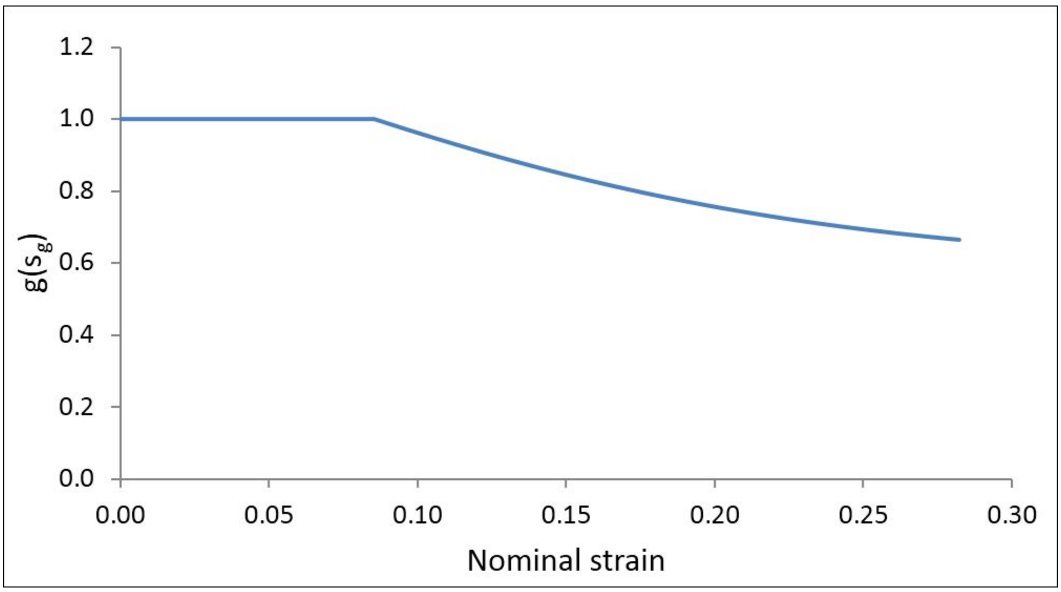

Figure 4.2. Damage function $g(s_g)$.

4.4. Unloading and Reloading Functions

The cyclic function was determined using the uniaxial single cycle test at 0.724 min^{-1} strain rate and 20 ^{o}C, Figure 6.11, where the specimen was loaded to 20% strain then unloaded to zero stress and then reloaded to failure. Unloading and reloading functions were determined by least-square curve fitting of Equation 4.2 to stress data. The resulting functions are shown in Figure 4.3.

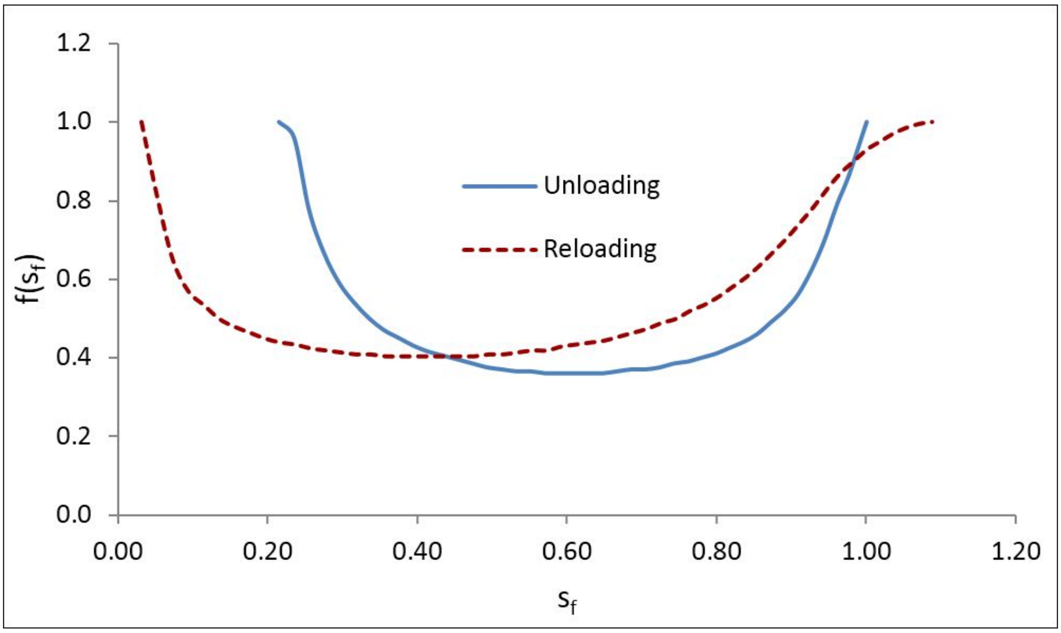

Figure 4.3. Unloading and reloading functions.

5. VERIFICATION OF THE CONSTITUTIVE MODEL IMPLEMENTATION

The implementation of the computational algorithm for nondamaging model presented in Chapter 3 was verified for different loading and boundary conditions by comparing the finite element analysis results to those obtained by using the finite strain viscoelastic constitutive model built-in ABAQUS. The results presented in this chapter were normalized according to the maximum value of the data in each test.

5.1. Homogeneous Deformation States

As an example of homogenous deformation, uniaxial constant strain rate tensile loading was considered. The model was verified for constant as well as transient temperatures. The mesh consisted of one full integration linear element.

5.1.1. Uniaxial Tension at Constant Temperature

The loading consisted of monotonous stretching at 0.001 min^{-1} strain rate and 50 $°C$. Symmetry boundary conditions were applied. Figure 5.1 shows undeformed and deformed states of the model. As seen in Figure 5.2 stress and dilatational responses of the developed model match exactly those of built-in ABAQUS model.

5.1.2. Uniaxial Tension at Transient Temperature

The loading consisted of stretching at 0.001 min^{-1} strain rate and simultaneously cooling from 50 $°C$ at the rate of 20 $°C/hour$. Symmetry boundary conditions were applied. Figure 5.3 shows that the stress response of the developed model matches exactly that of the built-in ABAQUS model.

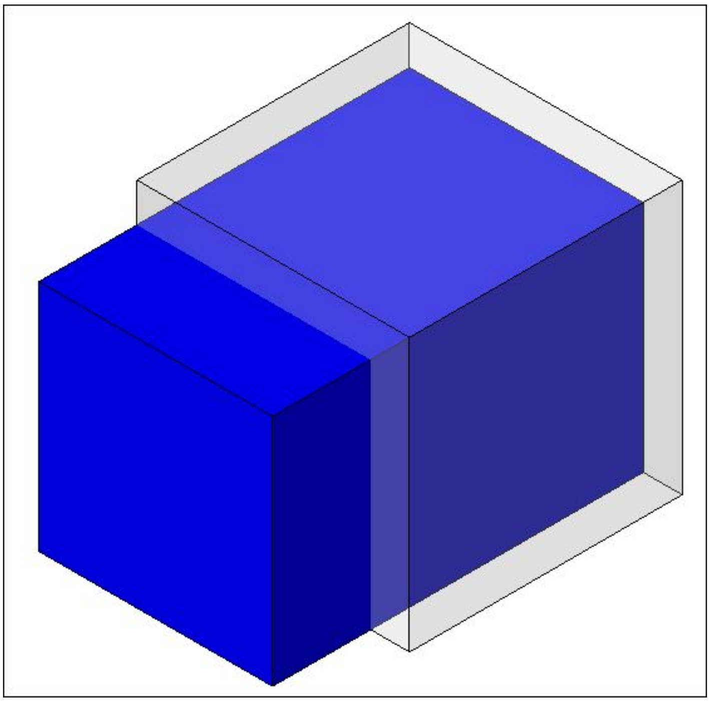

Figure 5.1. Deformed and undeformed meshes for uniaxial tension.

5.2. Complex Deformation States

The wedge model was used for verification of a multi-element mesh. The model represents an analogue cylindrical rocket motor with propellant grain and metal casing. The wedge represents one quarter of the geometry, hence symmetry boundary conditions were applied at the lateral and bottom surfaces. The mesh consisted of quadratic reduced integration elements as shown in Figure 5.4.

5.2.1. Pressure Loading

Only the grain was modelled. Pressure load of 0.7 MPa was applied to the inner surface. Figure 5.5 shows the deformed shape of the model and Figure 5.6 shows Mises stress history at the mid-top inner surface indicated in Figure 5.4. It is seen that the predictions compare well with those provided by built-in ABAQUS model.

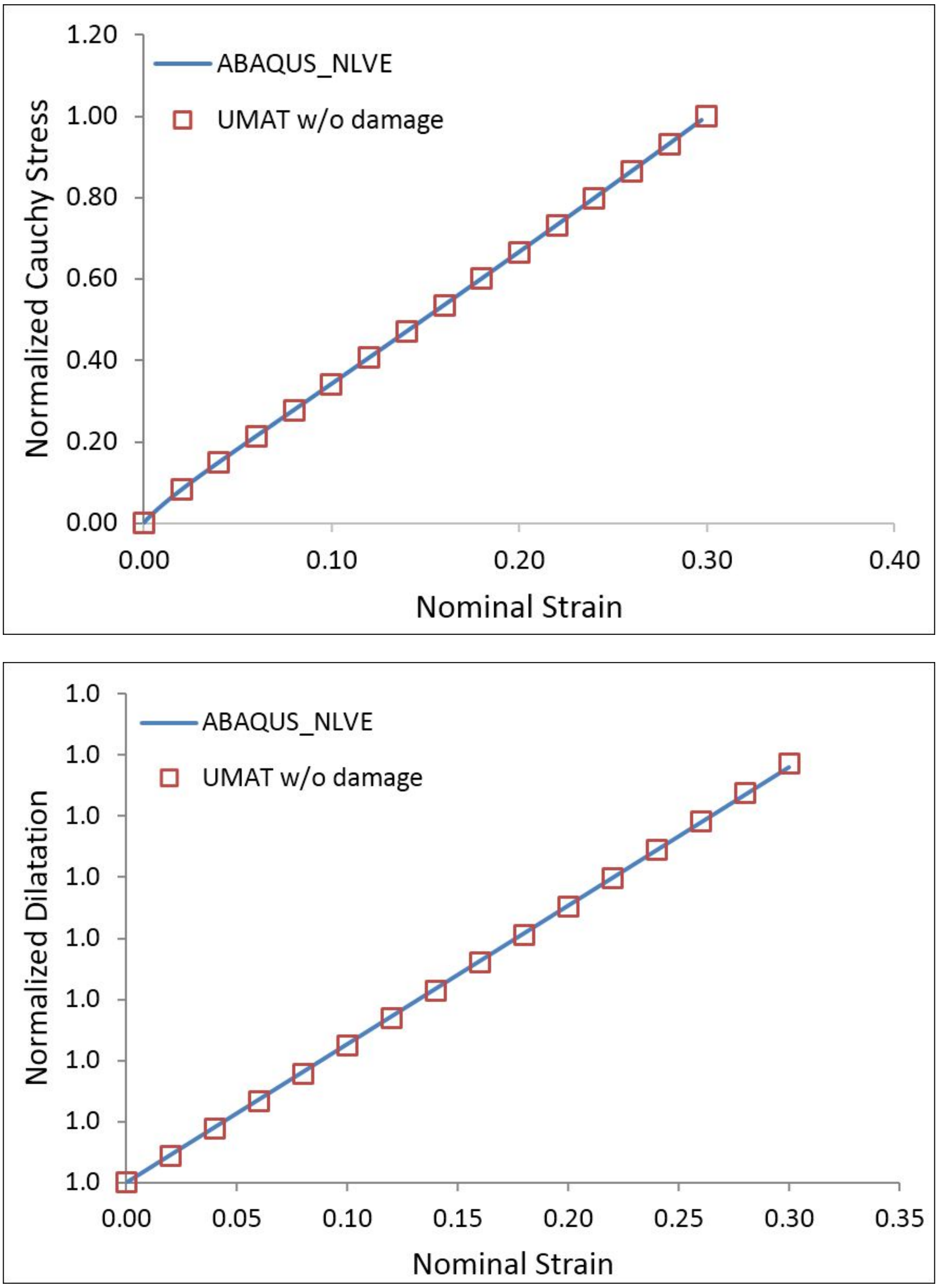

Figure 5.2. Stress and dilatation responses for uniaxial loading at 0.001 min^{-1} and 50 $^{\circ}C$.

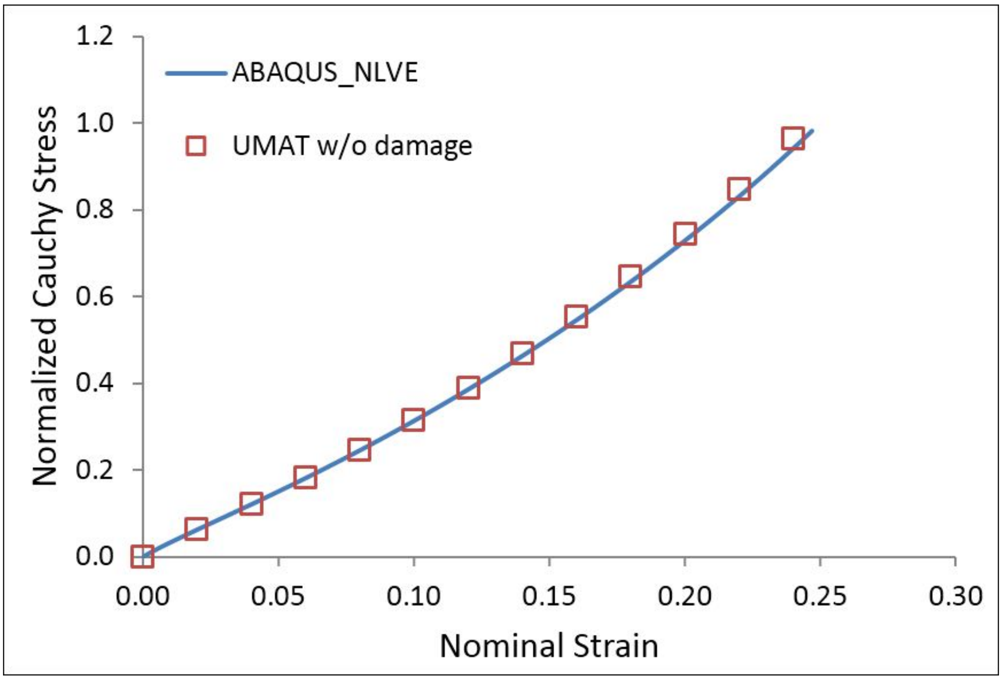

Figure 5.3. Stress response for simultaneous uniaxial loading at 0.001 min^{-1} and cooling from 50 $°C$ at 20 $°C/hour$.

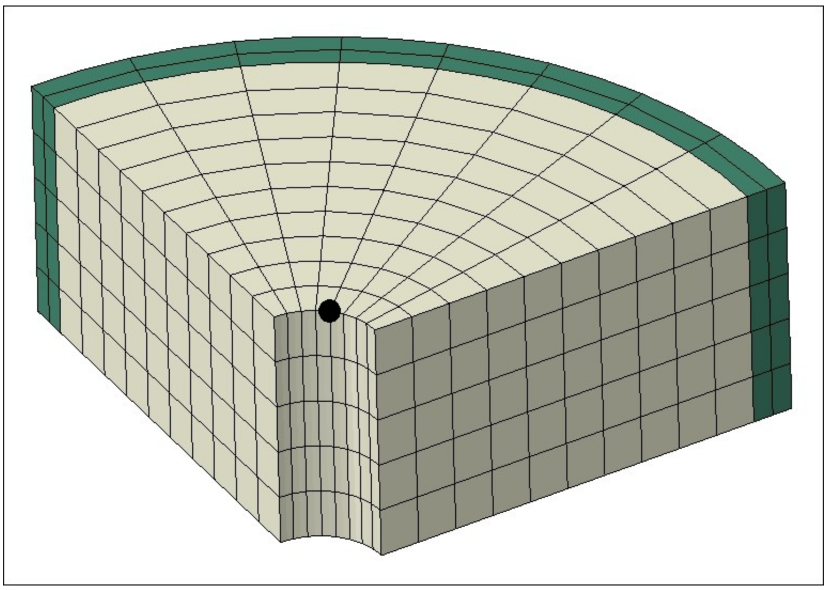

Figure 5.4. Wedge model mesh ("•" indicates the location where results for this model are presented).

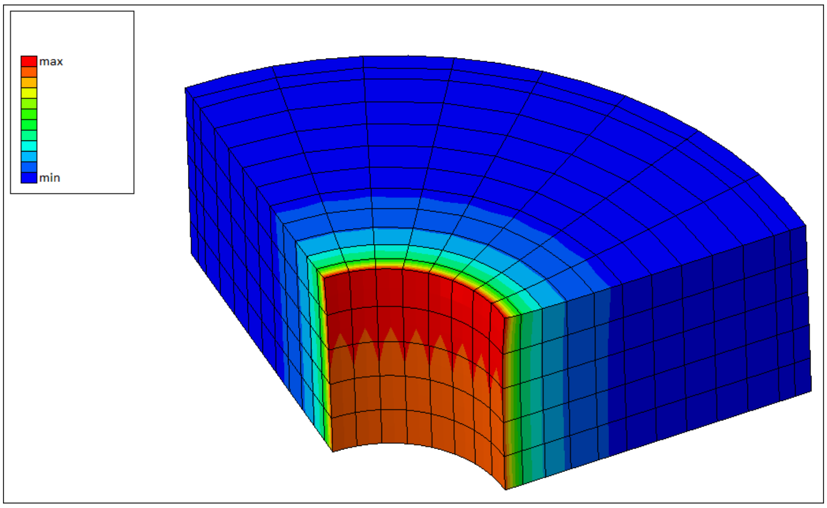

Figure 5.5. Deformed mesh of the wedge subjected to internal pressurization.

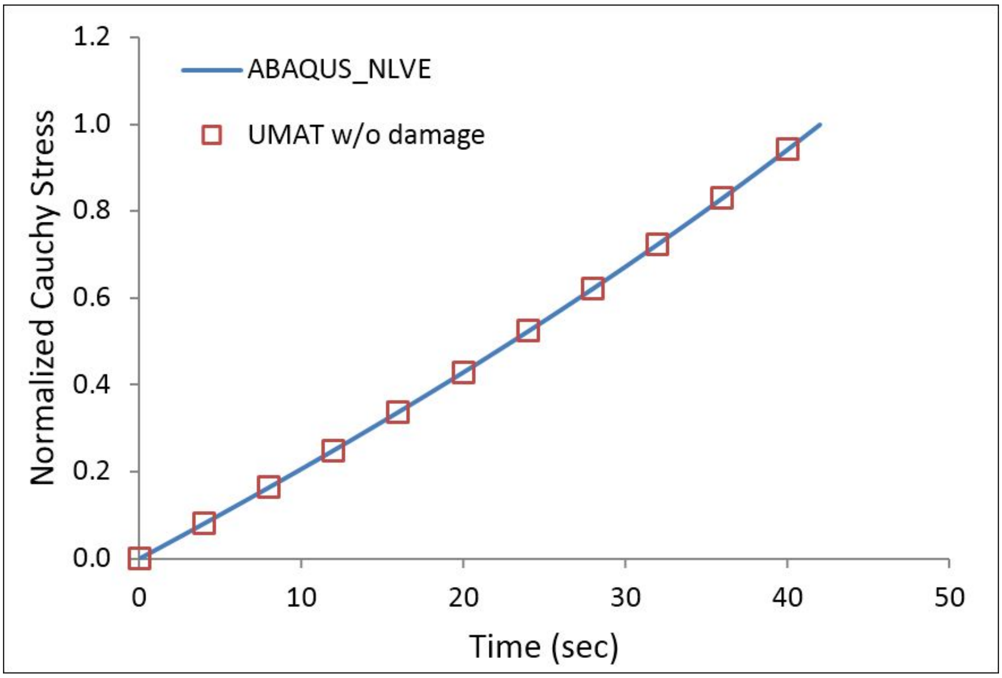

Figure 5.6. Stress response of wedge subjected to 0.7 MPa internal pressurization.

5.2.2. Thermal Loading

Both the grain and the steel casing were considered. The loading consisted of uniform cooling from initial temperature of 60 $°C$ at the rate of 20 $°C/hour$. Figure 5.7 shows that the Mises stress values at the bore, inner surface of the wedge, obtained from the implemented model and the built-in finite strain viscoelastic model compare very well.

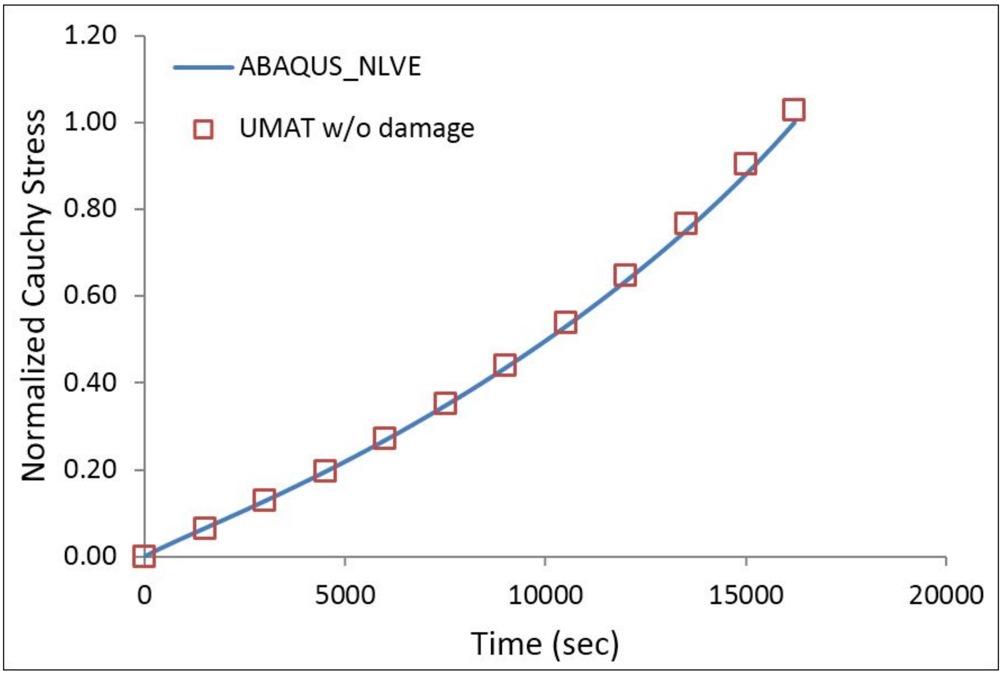

Figure 5.7. Stress response of wedge subjected to cooling from 60 $°C$ at 20 $°C/hour$.

5.2.3. Shear Loading

Both the grain and the steel casing were considered. 0.5 MPa shear load was applied to the inner surface of the wedge. Figure 5.8 shows deformed shape of the model. Figure 5.9 shows that the stress responses from the implemented model and the built-in finite strain viscoelastic model compare very well.

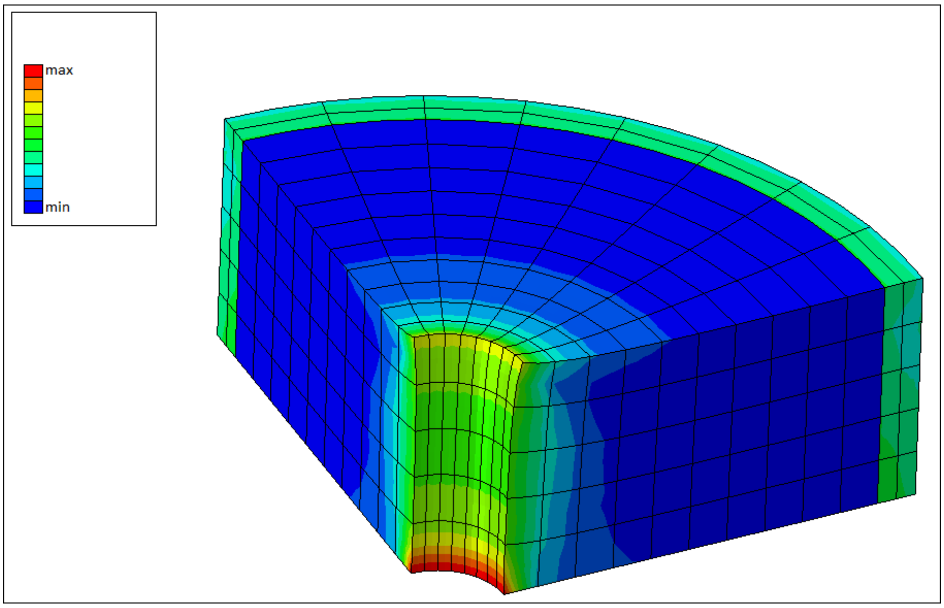

Figure 5.8. Deformed mesh of the wedge subjected to shear loading at the inner surface.

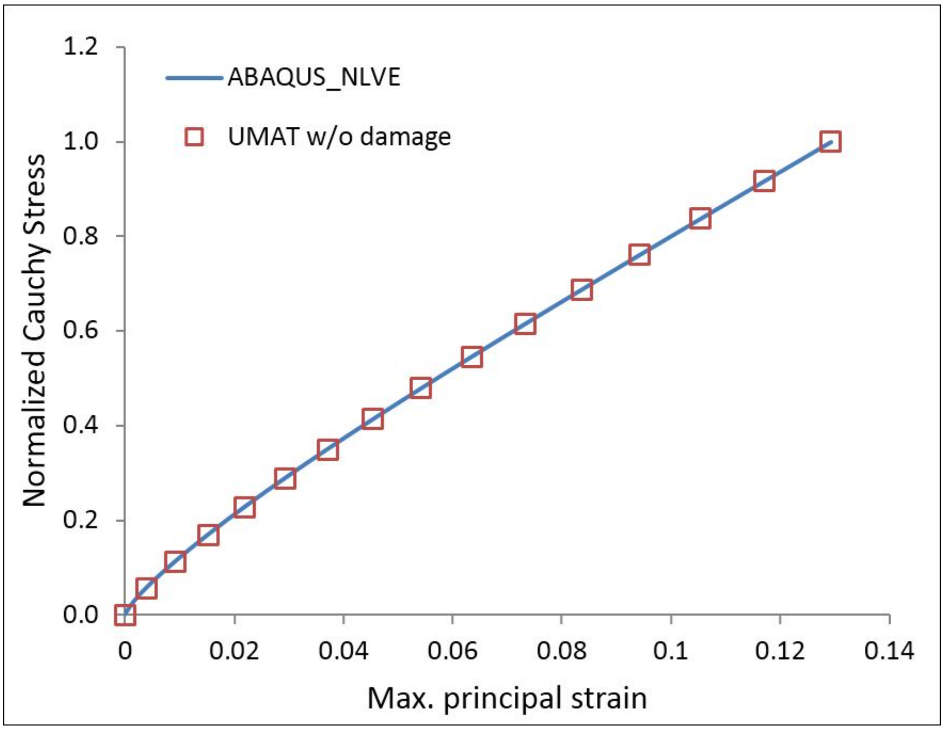

Figure 5.9. Stress response of wedge subjected to 0.5 MPa shearing.

5.3. Verification for Element Types

The material model implementation was verified for various three-dimensional elements. The wedge model introduced in Section 5.2 was used, and the pressure loading and boundary conditions presented in Sections 5.2.1 were applied. Figure 5.10 and Figure 5.11 show the stress results at the inner surface of the wedge model for quadratic full integration and linear full integration elements, respectively. The results compare well with those from built-in ABAQUS material model. The stress comparison of different element types is shown in Figure 5.12 for converged meshes. It is concluded that the mesh with linear elements results in lower stress values than the mesh with quadratic elements.

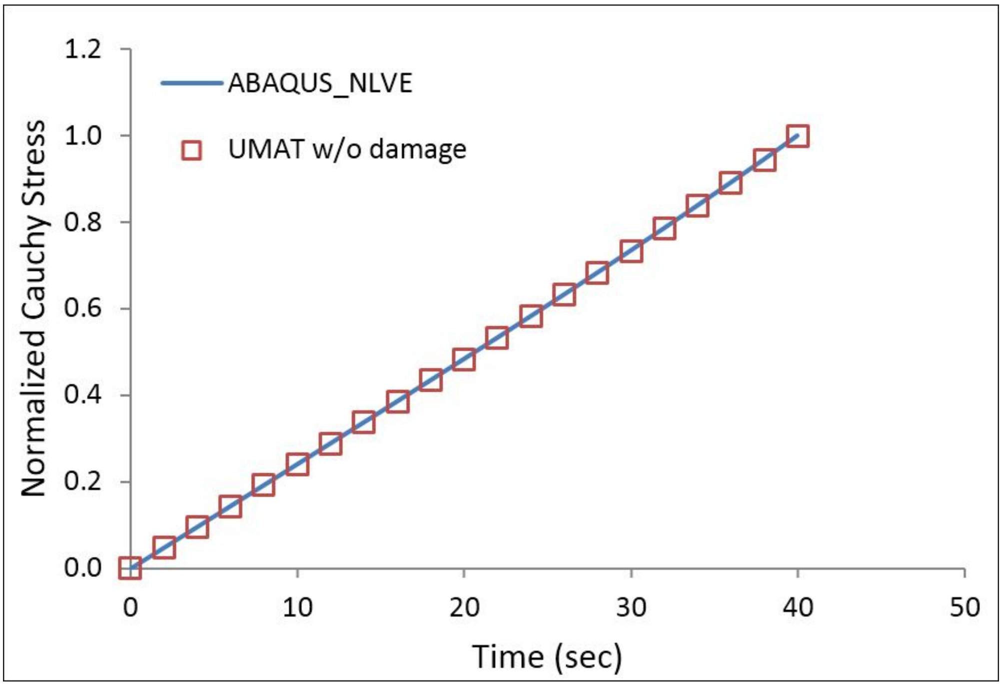

Figure 5.10. Stress response of wedge subjected to 0.7 MPa internal pressure: quadratic full integration elements.

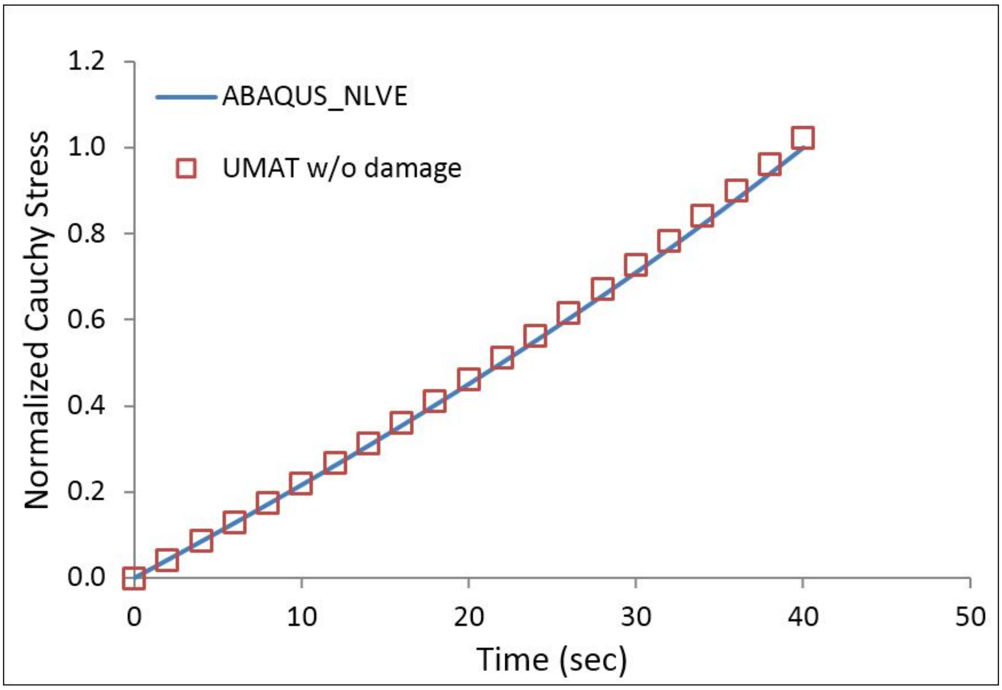

Figure 5.11. Stress response of wedge subjected to 0.7 MPa internal pressure: linear full integration elements.

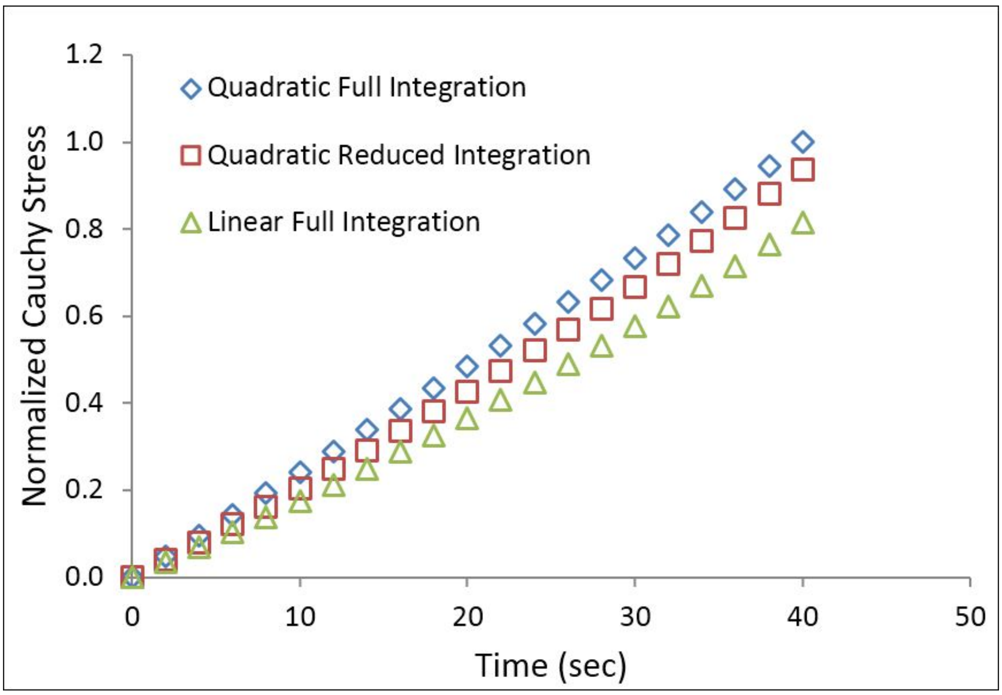

Figure 5.12. Stress response of wedge subjected to 0.7 MPa internal pressure: comparison of various element types.

6. VALIDATION OF THE CONSTITUTIVE MODEL

Predictions of the constitutive model are presented in this chapter. The implementation and the predictive capability of the damaging constitutive model were validated against test data. Uniaxial and biaxial monotonic and cyclic loadings were considered. Tests data at various loading rates, temperatures and superimposed pressure levels allowed extensive evaluation of the proposed model. The results presented in this chapter were normalized by the maximum value of data in each test.

6.1. Relaxation Test

Relaxation tests and the predictions at -40 $°C$, 0 $°C$, 20 $°C$ and 40 $°C$ are presented in Figure 6.1. The specimen was loaded to 0.02 strain at 0.00017 min^{-1} and then strain was fixed to observe stress relaxation. Predictions match test data well at 0 $°C$ and 20 $°C$. The mismatch at -40 $°C$ and 40 $°C$ may be attributed to the use of WLF form in representing the shift function. The effect of this mismatch is felt at uniaxial constant strain tests, in particular in those at low temperatures.

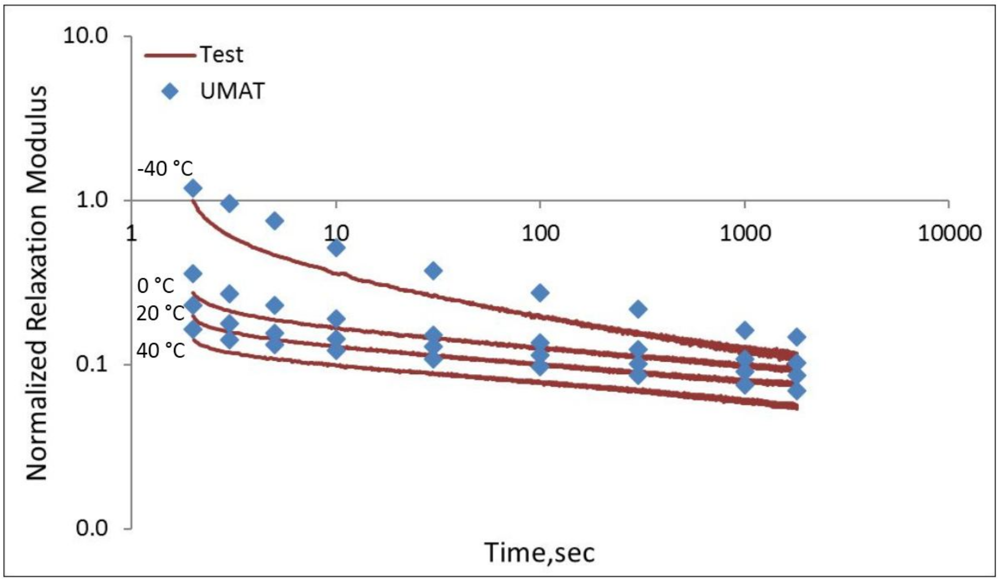

Figure 6.1. Relaxation modulus at various temperatures.

6.2. Constant Strain Rate Test

In constant strain rate tests presented in the following, specimens were loaded to failure at various rates. Tests given in Sections 6.2.1 and 6.2.2 were performed under constant temperature and pressure conditions, while those presented in Section 6.2.3 were performed under changing temperature and constant pressure.

6.2.1. Uniaxial Loading

Uniaxial loading stress and dilatation predictions and test data are shown in Figure 6.2 through Figure 6.4. Three levels of strain rate, lowest at 0.00724 min^{-1} and highest 10^3 times faster, were applied. Superimposed pressures consisted of 0, 1.75 and 6.45 MPa, the highest corresponding to the value at launch of the rocket. Test temperatures consisted of 20 $°C$ and -40 $°C$, the former representing the ambient value, the latter assumed to be the lowest value the material would be exposed in its lifetime. According to Figure 6.2, rate effect on the stress is represented reasonably at low to moderate rates, while slightly overpredicted at high strain rates. Constant strain test at 0.724 min^{-1} was used in model calibration, hence overlap of model and test results. Test data show little rate effect on dilatation response. This effect was not modelled in the constitutive equation, as a consequence dilatation predictions at different loading rates are close to each other. According to Figure 6.3, at -40 $°C$ stress is overpredicted at moderate and high strain rates. This is in accordance with the overpredicted stress relaxation at -40 $°C$ as shown in Figure 6.1. A possible explanation is that thermorheologically simple behaviour is not completely valid for this material since the stress is overpredicted over the entire range of test including low strain region where damage has not yet started. The overlap of the predictions and test data at the lowest strain rate shown in Figure 6.3 needs to be interpreted with caution since this may be a consequence of model's overprediction at low temperatures, in this case -40 $°C$ and 0.00724 min^{-1}. Figure 6.4 shows that the effect of superimposed pressure is represented well for dilatational response and reasonably well for stress response.

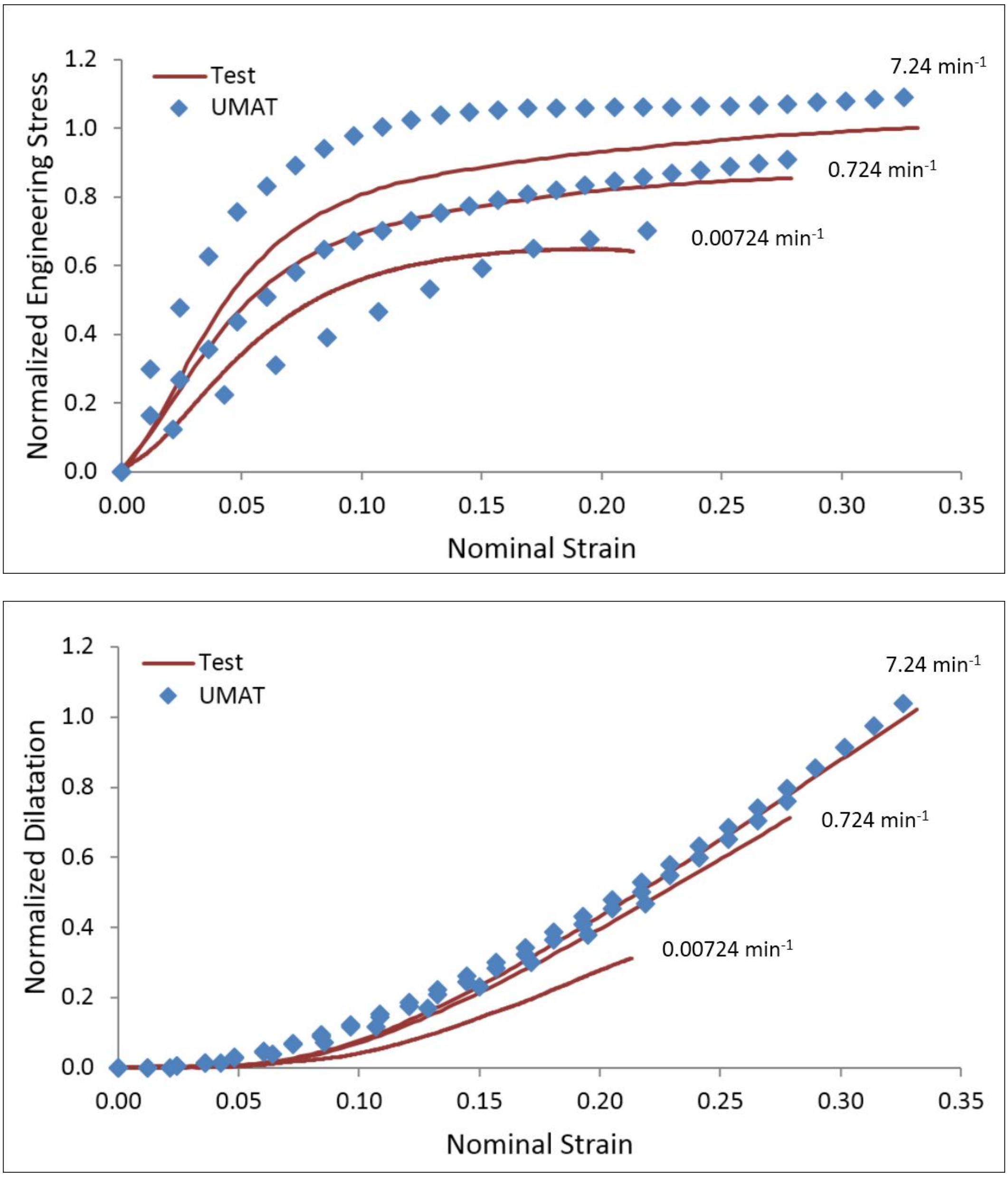

Figure 6.2. Uniaxial constant strain rate tests at 20 $°C$.

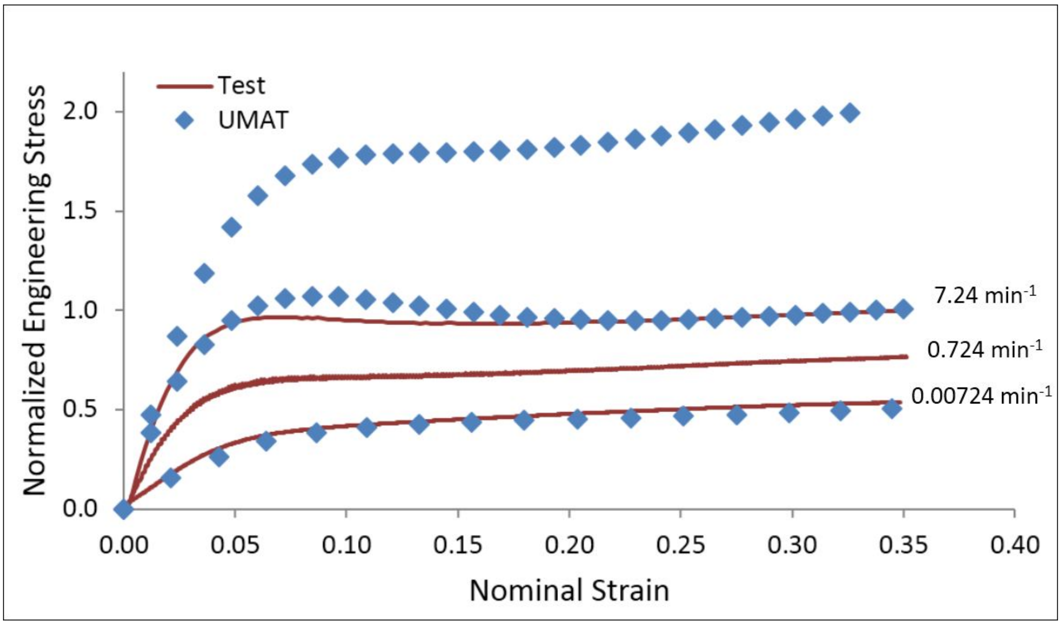

Figure 6.3. Uniaxial constant strain rate tests at -40 $°C$.

6.2.2. Biaxial Loading

Biaxial loading predictions and tests are shown in Figure 6.5. Loading was applied at strain rate of 0.724 min^{-1}, at 20 $°C$ and 0 $°C$ and ambient pressure. The stress predictions compare well with the test data at 20 $°C$, and are slightly overpredicted at 0 $°C$.

6.2.3. Uniaxial Loading at Transient Temperature

The test results and predictions for the simultaneous straining-cooling and straining-heating are presented in this section. One element model was used to perform straining and cooling simulation. In order to validate the damaging model and computational algorithm, finite element model of the test specimen was prepared and was used in straining-heating simulation.

<u>6.2.3.1. Straining and Cooling Test.</u> The results of simultaneous straining-cooling simulation and the test data are shown in Figure 6.6. The loading consisted of uniaxial

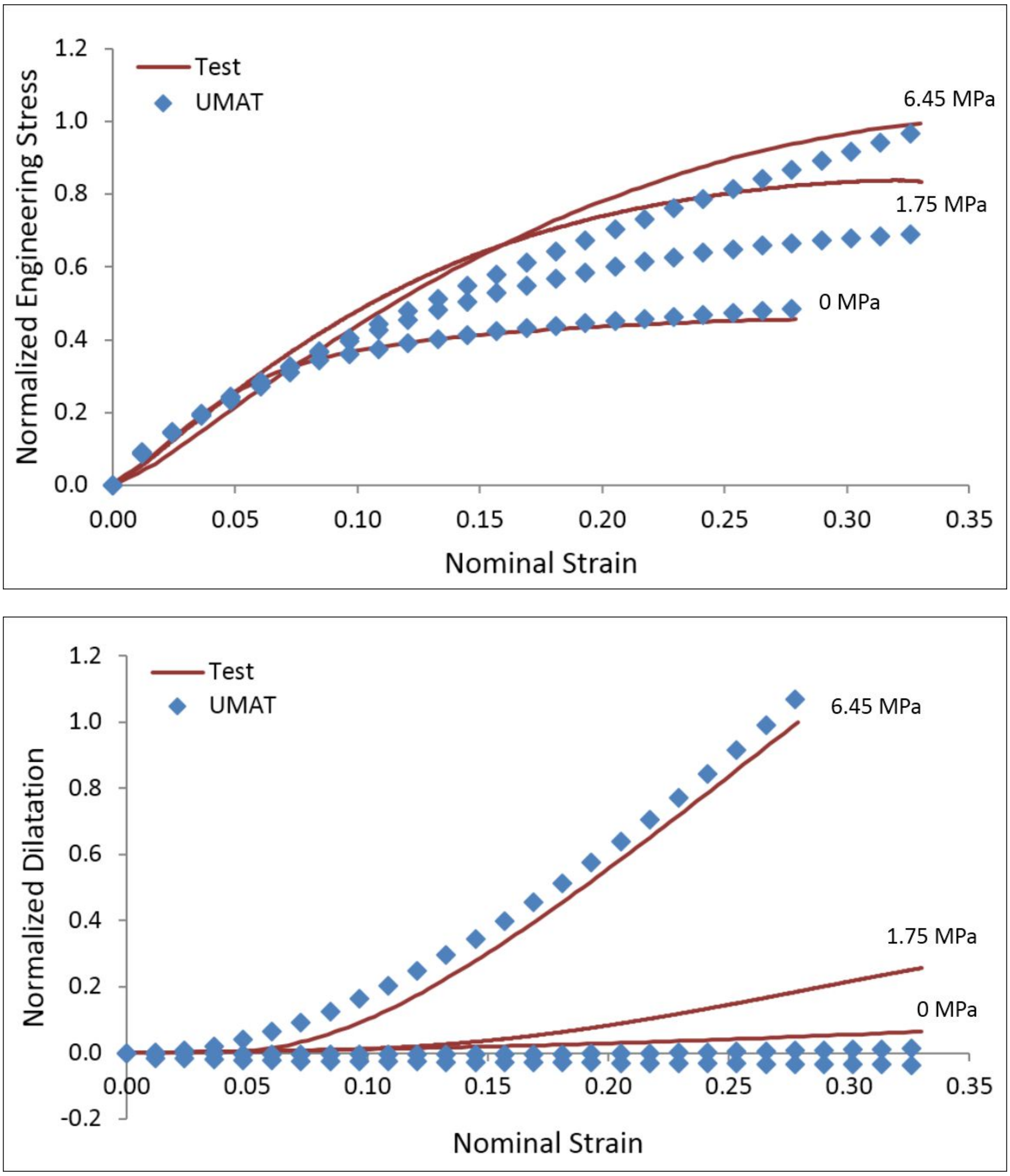

Figure 6.4. Uniaxial constant strain rate tests under superimposed pressures at 0.724 min^{-1} and 20 $°C$.

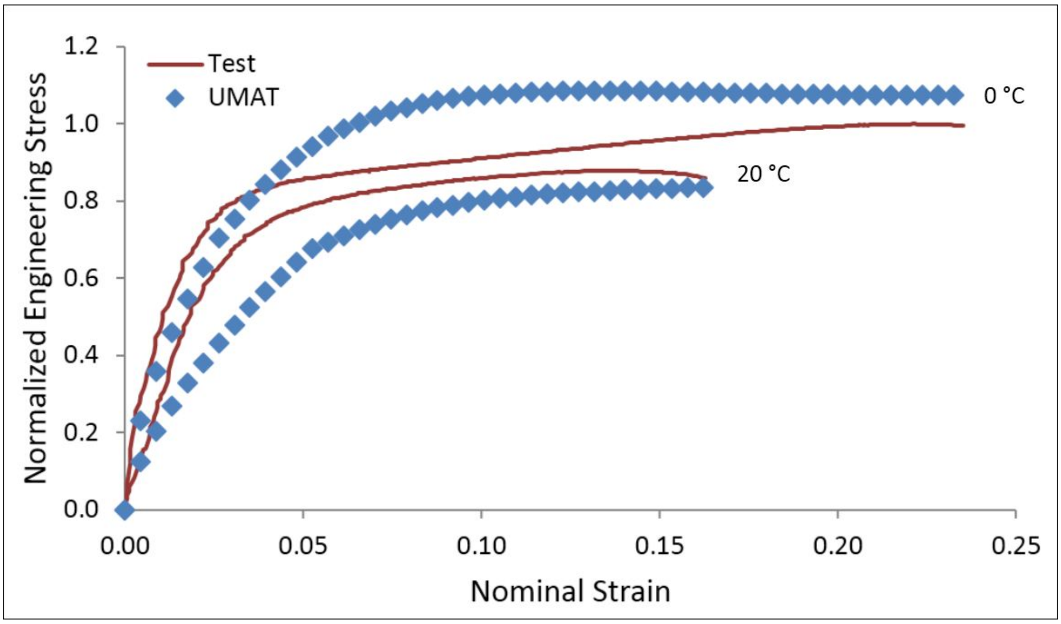

Figure 6.5. Biaxial constant rate tests at 0.724 min^{-1} and at 0 $°C$ and 20 $°C$.

straining at 0.001 min^{-1} while temperature was decreased from 50 $°C$ at 15 $°C/hour$. It is observed that the predictions are quite reasonable when compared to test data. The difference in results is a consequence of under prediction in the low strain region where the effect of damage in negligible. This is most likely due to the thermorheologically complex behaviour of the propellant and underprediction of the response at low rates as they were indicated in the uniaxial constant strain rate tests.

6.2.3.2. Straining and Heating Test. A finite element model representing the uniaxial test specimen geometry was developed to perform simultaneous straining-heating simulation. Only one quarter of the specimen was modelled and symmetry boundary conditions were applied to the lateral and bottom surfaces of the geometry. The mesh consisted of quadratic reduced integration elements and is shown in Figure 6.7. The loading consisted of uniaxial straining at 0.001 min^{-1} while increasing temperature from -40 $°C$ at 15 $°C/hour$. The prediction of the finite element model and the result of test data are shown in Figure 6.8. The engineering stress was calculated from the reaction force divided to undeformed cross-section area of the specimen and the nominal strain in the loading direction was obtained from the integration point of the

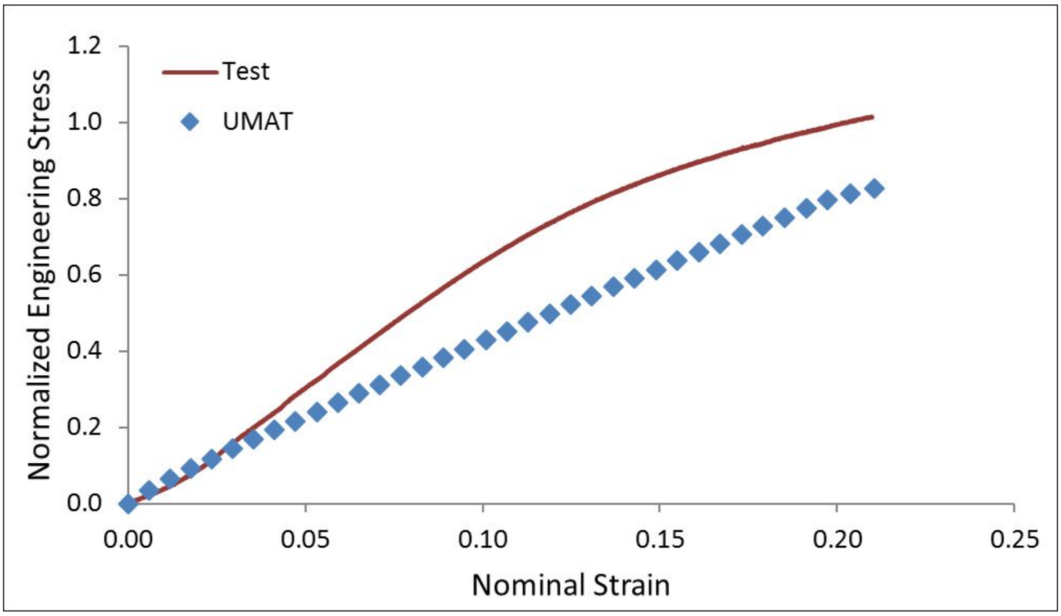

Figure 6.6. Stress response of tensile test specimen model subjected to simultaneous straining at 0.001 min^{-1} and cooling from 50 $°C$ at 15 $°C/hour$.

element on the symmetry plane. Uniaxial engineering strain ϵ

$$\epsilon = \lambda - 1 \tag{6.1}$$

was computed from the logarithmic strain $\epsilon_L = \ln\lambda$ provided by ABAQUS according to

$$\epsilon = e^{\epsilon_L} - 1 \tag{6.2}$$

The predictions compare quite reasonably with the test data. The model underpredicts the test data as in the case of straining-cooling simulation due to once again the thermorheologically complex behaviour of the propellant and the underprediction of the response at low rates. Distributions of Von Mises stress, damage function $g(s_g)$ and void content $c(t)$ are shown in Figure 6.9. It is observed that both stress and state variables have smooth distributions. It is therefore concluded that the model and computational algorithm is robust and stable during three dimensional stress analysis

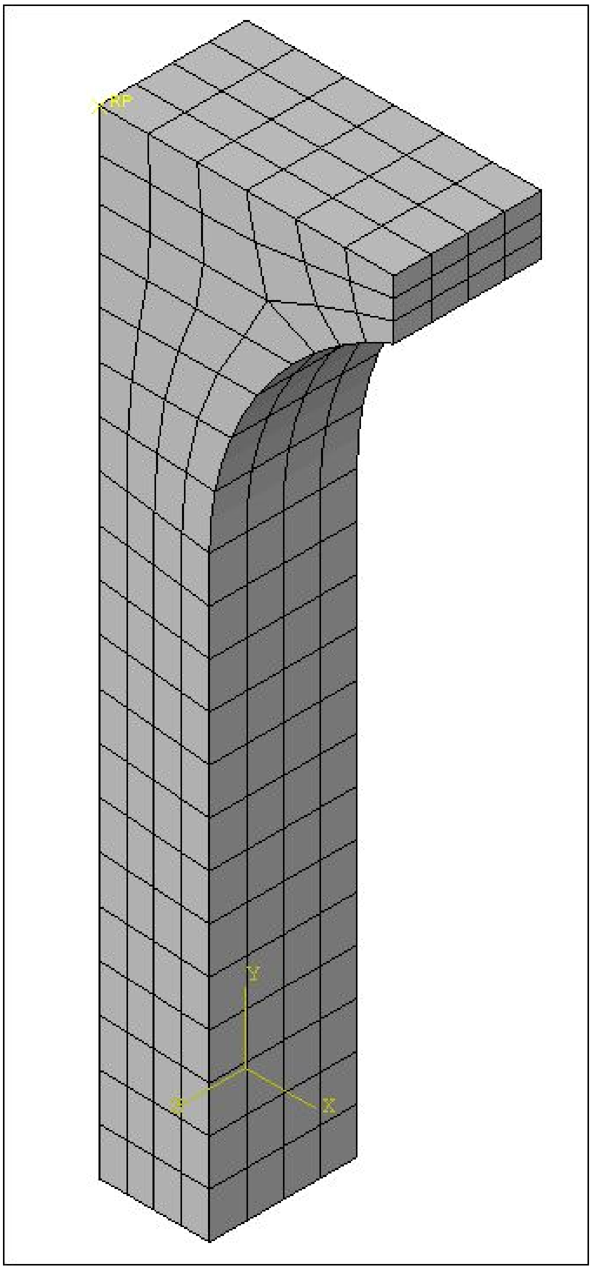

Figure 6.7. Finite element model of a uniaxial tensile test specimen.

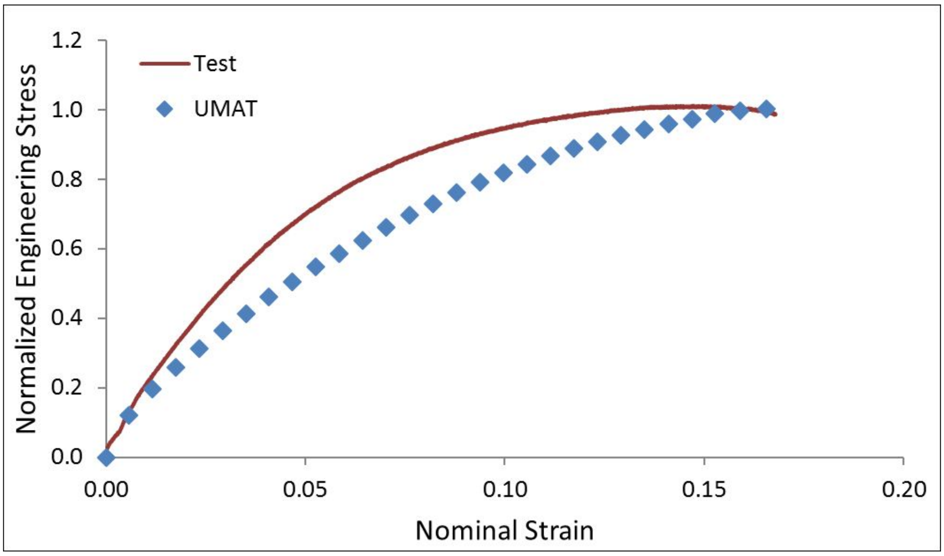

Figure 6.8. Simultaneous straining at 0.001 min^{-1} and heating from -40 $°C$ at 15 $°C/hour$.

of multi-element geometries.

6.3. Dual Strain Rate Test

Dual strain rate results are shown in Figure 6.10. The uniaxial specimen was initially loaded at 0.724 min^{-1}, upon reaching 11% strain, the rate was decreased to 0.0724 min^{-1}. The temperature was kept at 20 $°C$ throughout the entire loading. Predictions match the test data quite well.

6.4. Cyclic Test

Cyclic loadings are important for propellant modelling since the rocket motors are exposed to daily and annual cyclic temperature loading during storage. Figure 6.11 and Figure 6.12 show the two different loading scenarios that were used to determine the predictive capability of the model. Both loadings were applied at 0.724 min^{-1} and 20 $°C$. Single cycle loading shown in Figure 6.11 was used in the calibration of the unloading-reloading softening function, hence an excellent stress agreement is obtained.

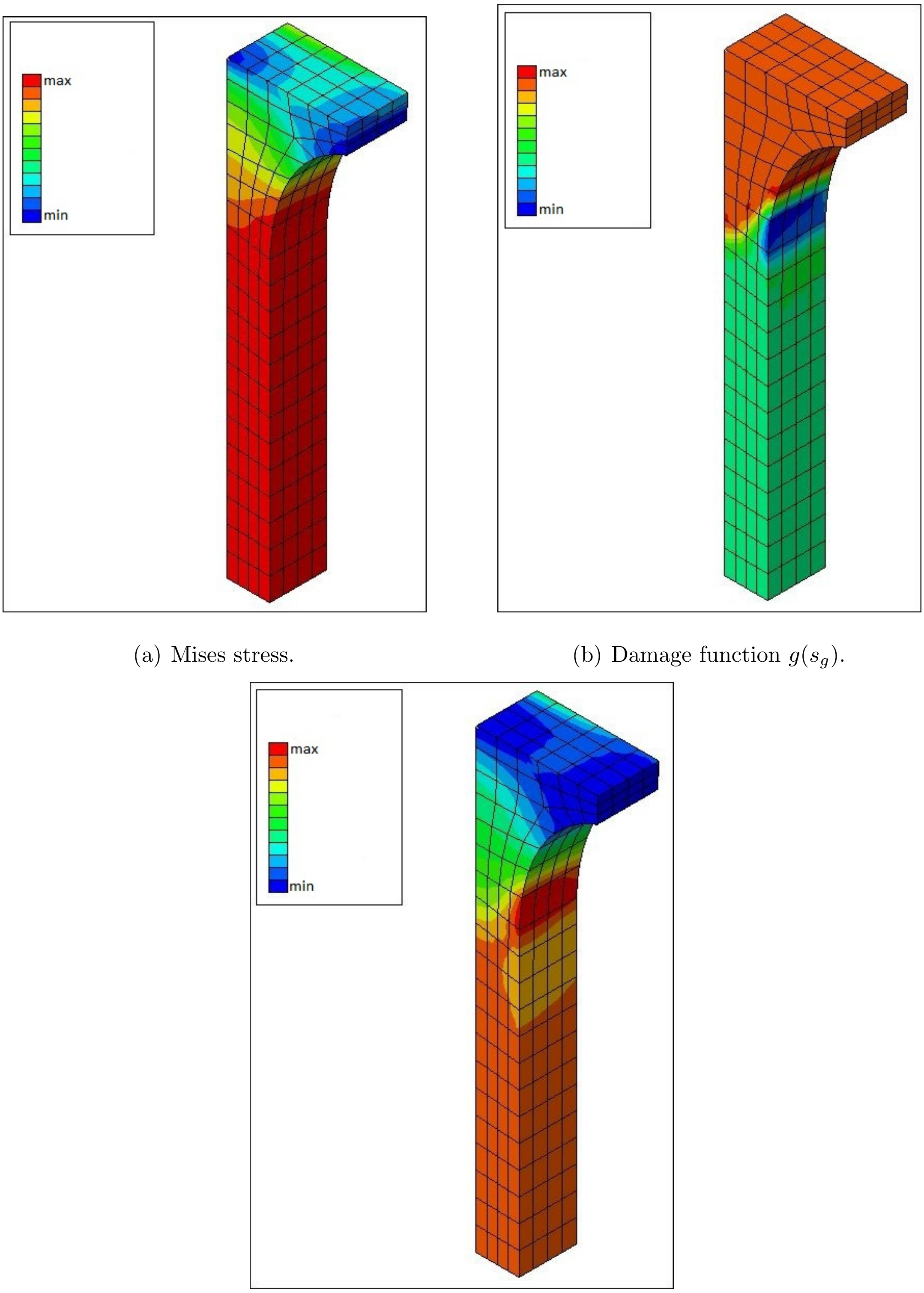

(a) Mises stress.

(b) Damage function $g(s_g)$.

(c) Void content $c(t)$.

Figure 6.9. Contour plots of Von Mises stress and damage model variables.

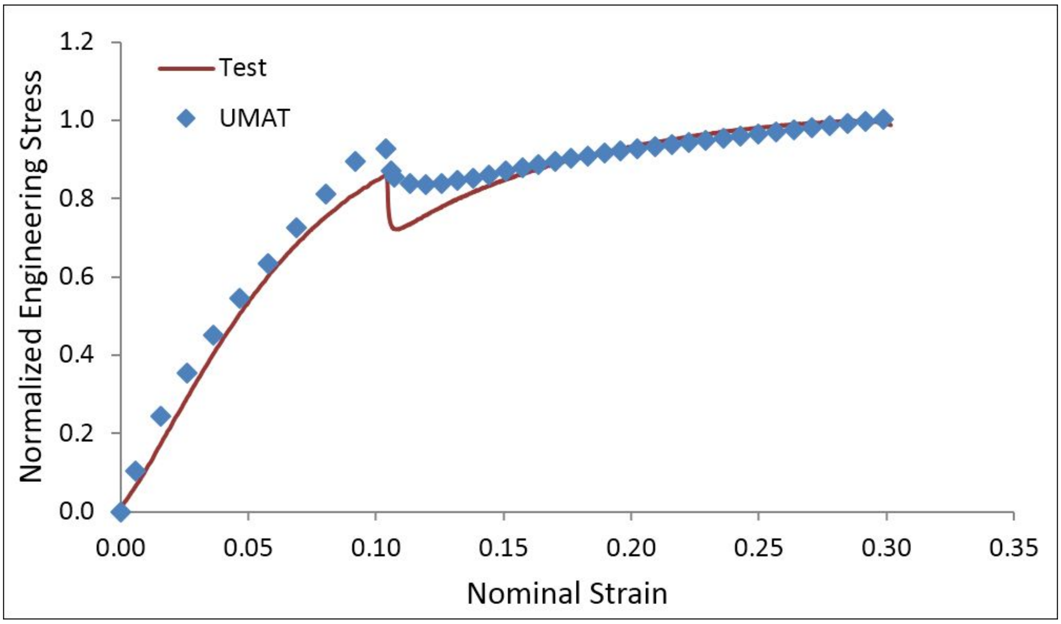

Figure 6.10. Dual strain rate test at 0.724 min^{-1} to 11% strain and 0.0724 min^{-1} to 30% strain at 20 $°C$.

The agreement of the dilatational response is entirely due to good predictive capability of the model. Figure 6.12 shows a multiple cycle loading to 20% strain. Both stress and dilatation responses are well predicted. An important observation is that introducing cyclic function as a multiplier to viscoelastic stress prevented the stress jumps on the stress response during the transition from unloading to loading phases. This approach also prevented numerical convergence problems with complex finite element meshes under cyclic thermal loading, as discussed in the next chapter.

6.5. Complex Loading

Complex history test consisted of loading and unloading at different strain rates and stress relaxation in between them. The first step was loading at 0.0068 min^{-1} up to 15% strain. The second step was relaxation for 10 minutes. The next step was unloading at 0.11 min^{-1} up to 5% strain followed by another relaxation for 10 min. The final loading was at 0.068 min^{-1} up to failure. The results are shown in Figure 6.13. Overall the predictions agree well with the test data.

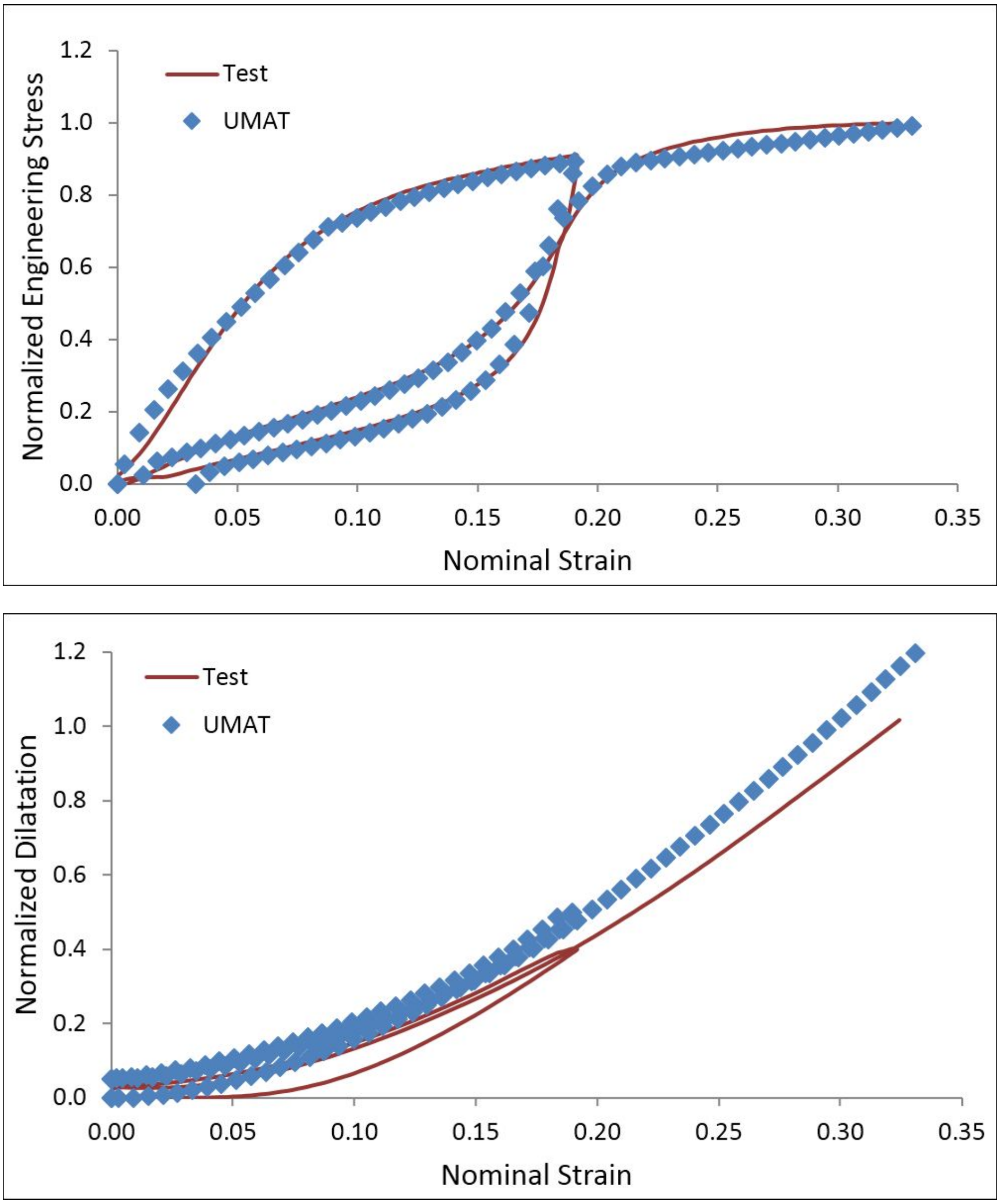

Figure 6.11. Uniaxial cyclic tensile test at 0.724 min^{-1} and 20 $^{\circ}C$ with one cycle at 20% strain.

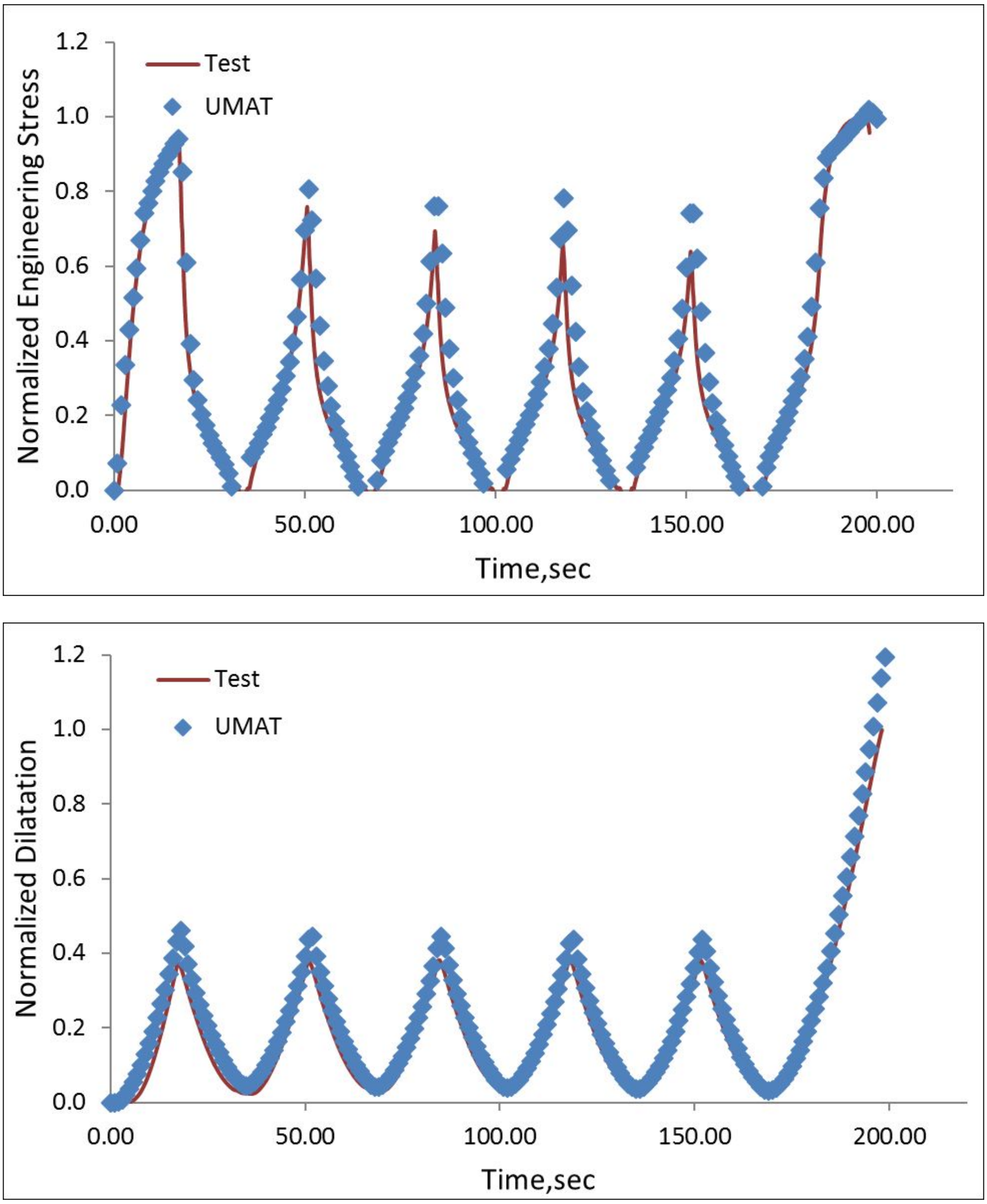

Figure 6.12. Uniaxial cyclic tensile test at 0.724 min^{-1} and 20 $^{\circ}C$ with five cycles at 20% strain.

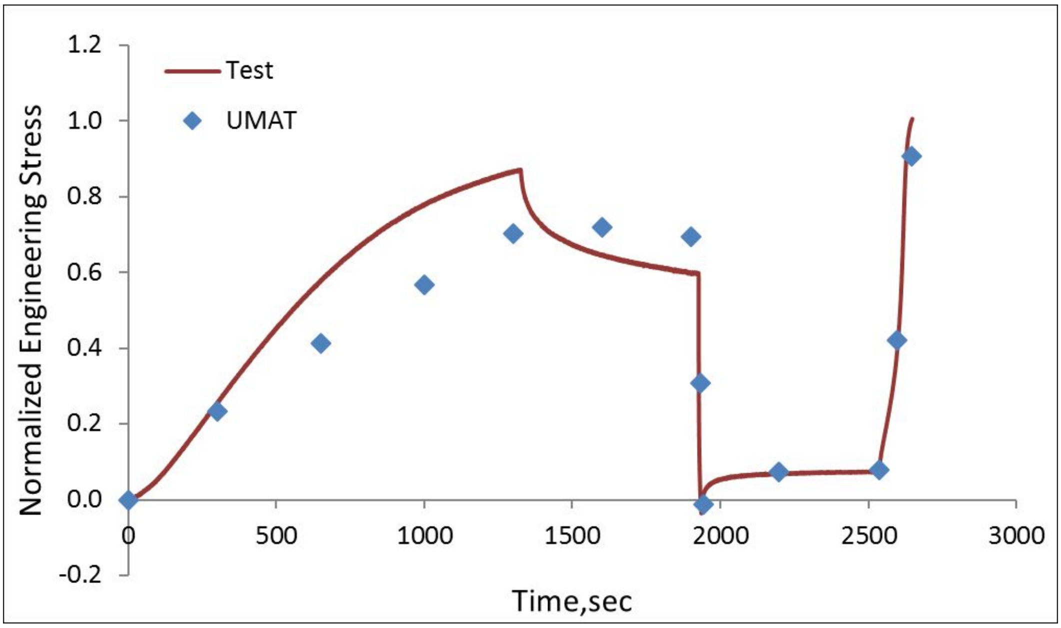

Figure 6.13. Uniaxial complex loading at 20 $^{\circ}C$.

7. THERMAL CYCLIC ANALYSIS OF ROCKET MOTOR

Rocket motor is typically exposed to annual and daily temperature variations during storage. Sudden temperature changes may also occur while the motor is in transfer. The cyclic temperature loading plays an important role on the fatigue life of solid propellant, since the material response is highly temperature dependent. As a consequence, for accurate prediction of the service life the determination of stress and strain field of the motor under cyclic thermal loading is essential. Depending on the complexity of the motor geometry, the interaction between the propellant grain and the other components of the motor and the nonlinearity of the constitutive model, convergence difficulties may occur in the finite element analysis.

In this section, finite element modelling of a rocket motor subjected to cyclic temperature loading is presented. The material model and the computational algorithm presented in previous sections were used to perform the stress analysis. In the following, first, the finite element model is detailed. Then various results regarding predictions under thermal cyclic analysis are presented. The predictions are compared to the test data obtained by dual bond stress and temperature sensor (DBST sensor) located at the interface of the propellant grain and the steel casing. Distribution of stress and constitutive model state variables are demonstrated.

7.1. Three Dimensional Model of A Rocket Motor

The rocket motor analyzed consisted of the propellant grain and steel casing. A three dimensional finite element model representing the motor was developed for the stress analysis. Due to symmetry considerations only one quarter of the specimen was modelled. The mesh is shown in Figure 7.1. Three dimensional quadratic reduced integration elements were used to construct the finite element mesh. Symmetry boundary conditions were applied at x, y and z planes of the model.

Mechanical properties resulting from the calibration outlined in Chapter 4 were used for the propellant. Typical steel properties were used for the casing. The coefficients of thermal expansion for the propellant and the casing differed by an order of magnitude. Temperature history shown in Figure 7.2 was uniformly applied to all of motor assembly during stress analysis. The temperature history in Figure 7.2 was normalized by the maximum value of temperature in the history.

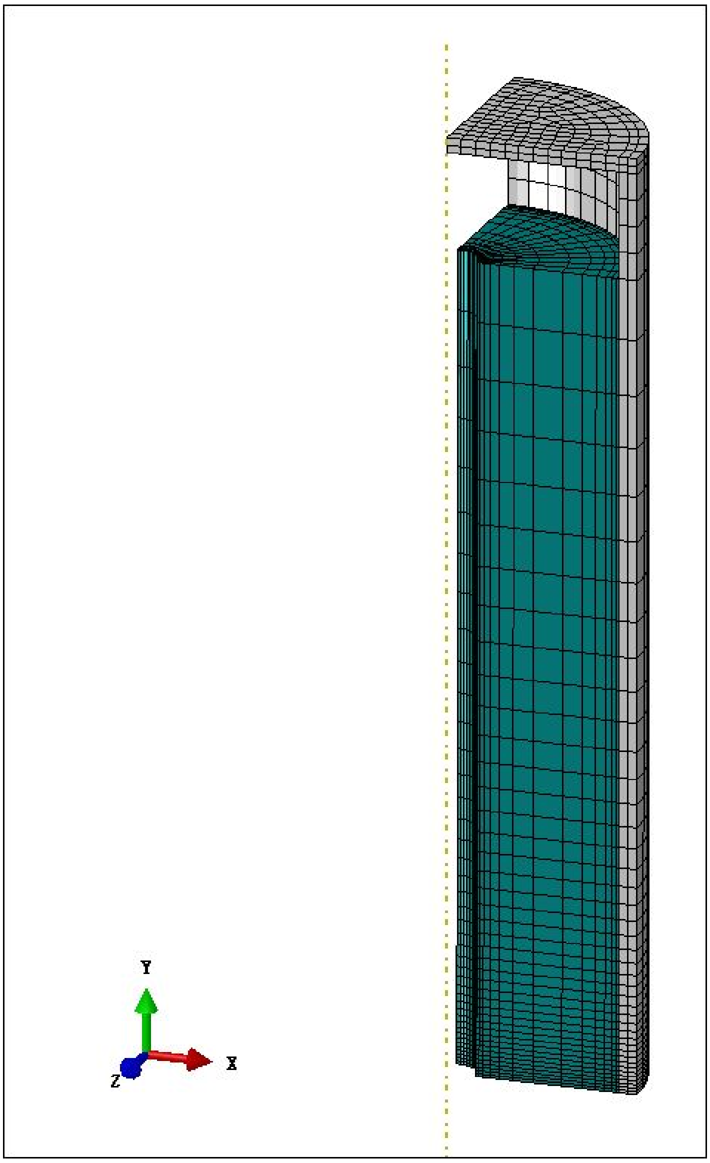

Figure 7.1. Rocket motor model: steel casing and solid propellant grain.

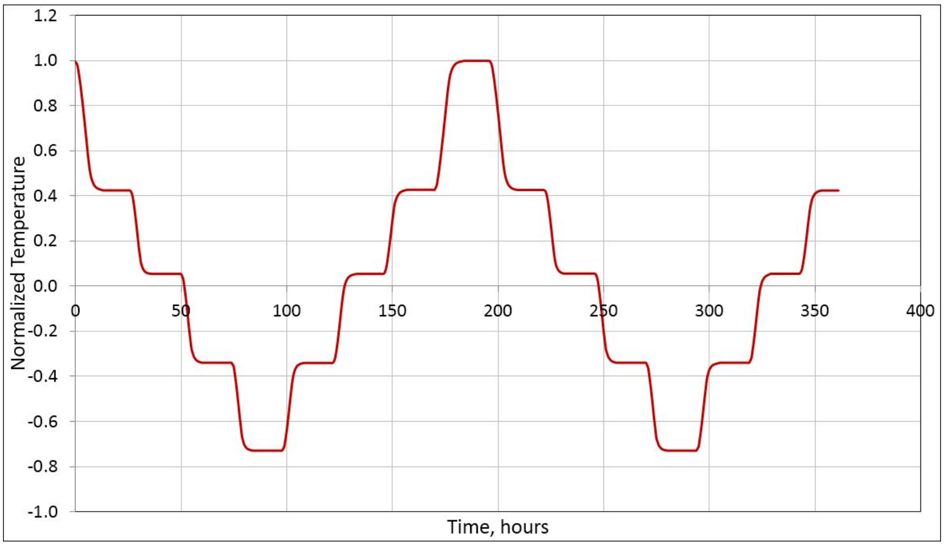

Figure 7.2. Temperature history.

7.2. Results

The distribution of Von Mises stress field on the rocket motor model and the grain only at the last time increment of the cyclic thermal stress analysis are shown in Figure 7.3. Maximum Mises stress is obtained at the bore at y-symmetry plane. Octahedral strain $I_\gamma(t)$ is shown in Figure 7.4a. Distribution of $I_\gamma(t)$ and the location of its maximum value are similar to that of Mises stress. Figure 7.4b shows the contour plot of void content, $c(t)$. Since the amount of void $c(t)$ is directly proportional to octahedral strain $I_\gamma(t)$, distribution of voids is similar to that of octahedral strain field and the maximum amount of void is formed at the bore at y-symmetry plane. Inversely, since bulk modulus decreases with increasing amount of void content, the value of bulk modulus is at its minimum at that location. Distribution of the bulk modulus $K(t)$ throughout the model is shown in Figure 7.4c. All of the contour plots show smooth variation of the variables. Based on the consistency of results with respect to expectations it is concluded that the material model and the computational algorithm are capable of predicting the behaviour of the rocket motor under cyclic thermal loading.

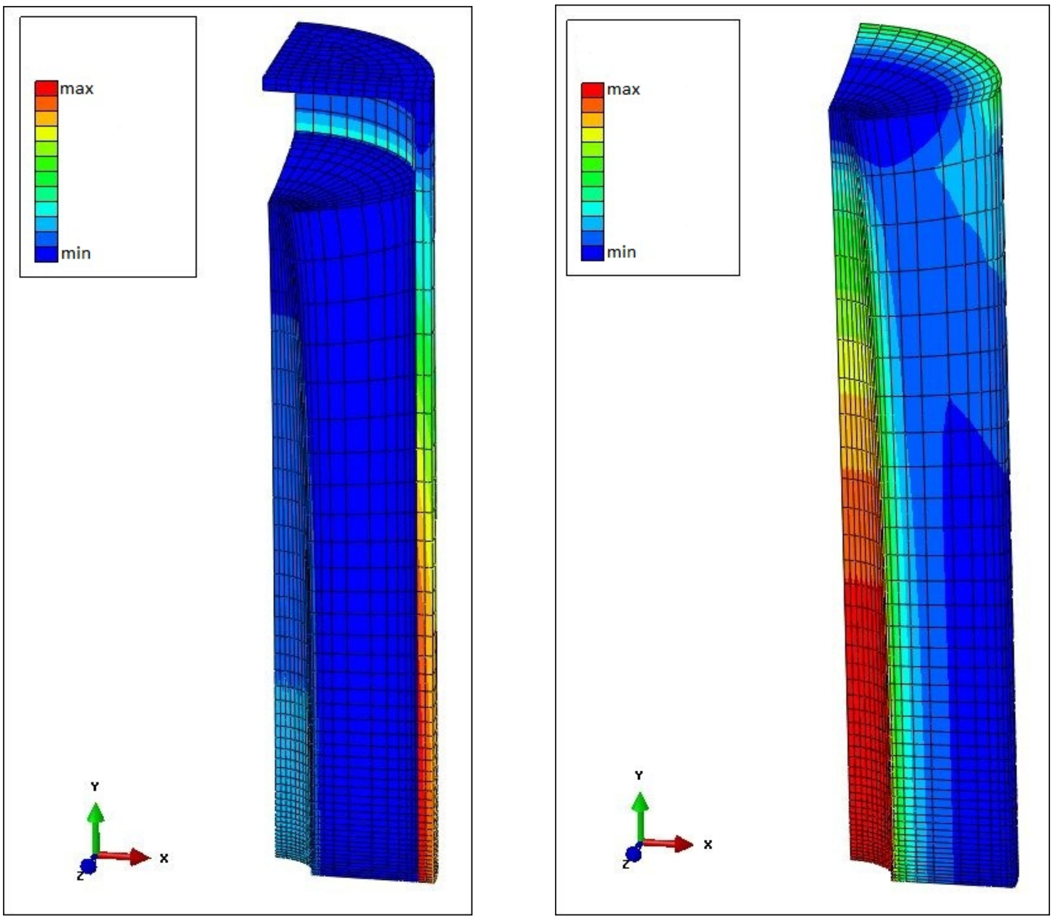

(a) Steel casing and grain.

(b) Grain.

Figure 7.3. Von Mises stress distribution at the last time increment.

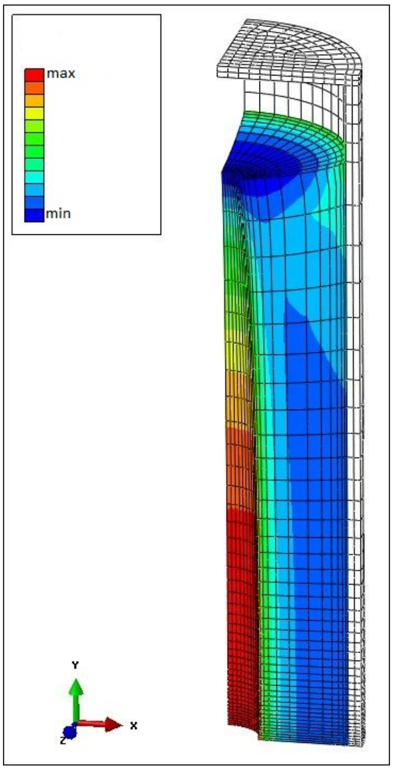

(a) Octahedral shear strain $I_\gamma(t)$.

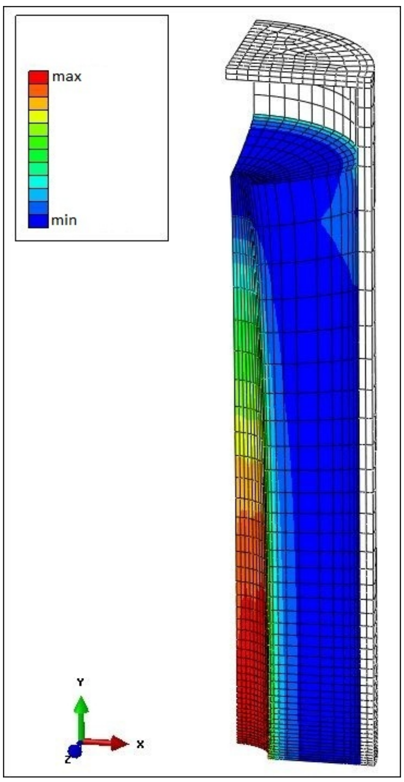

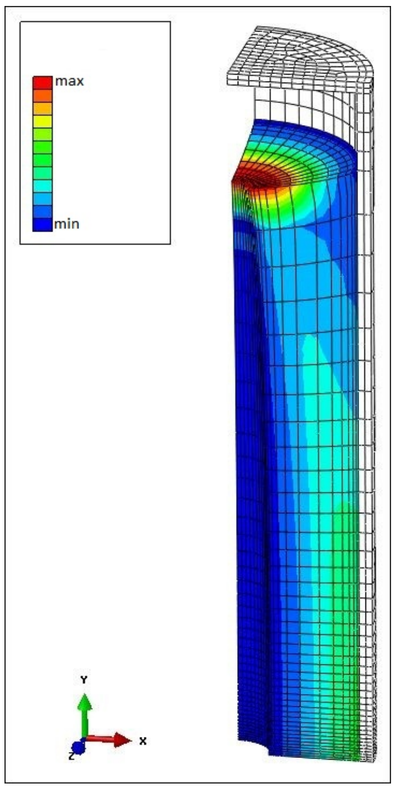

(b) Void content $c(t)$.

(c) Bulk modulus $K(t)$.

Figure 7.4. Contour plots of state variables at the last time increment.

Dual bond stress and temperature sensor (DBST sensor) was used to collect data during thermal cyclic test [24]. An element of the propellant grain which is at the same location as DBST sensor was chosen to evaluate the results of stress and state variables. The element where bond stress was evaluated is shown in Figure 7.5. The predicted history of stress response of the motor along with the experimental measurements and the results of built-in ABAQUS model are shown in Figure 7.6. All of the stress data were normalized by the maximum value of the stress reached in the test data. The results of only two cycles were plotted due to limited availability of the test data. As can be seen in Figure 7.6 the peak stress reached in each load cycle decreases from first cycle to the next for both test data and proposed model while it does not change for built-in ABAQUS model. This feature of the proposed model is due to the cyclic softening function $f(s_f)$ shown in Figure 7.7. Built-in ABAQUS model does not have capability to include softening effects during unloading and reloading. It should be noted that the proposed model predicts the softening of the maximum stress only in the second cycle. After second cycle no further decrease in the peak stress will be predicted.

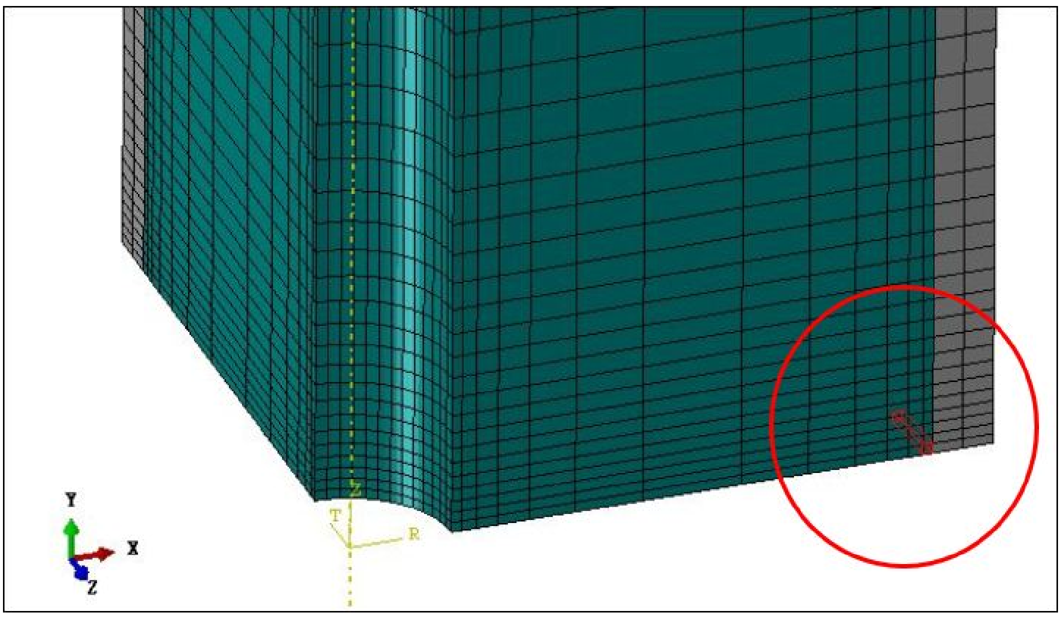

Figure 7.5. Element where bond stress was evaluated.

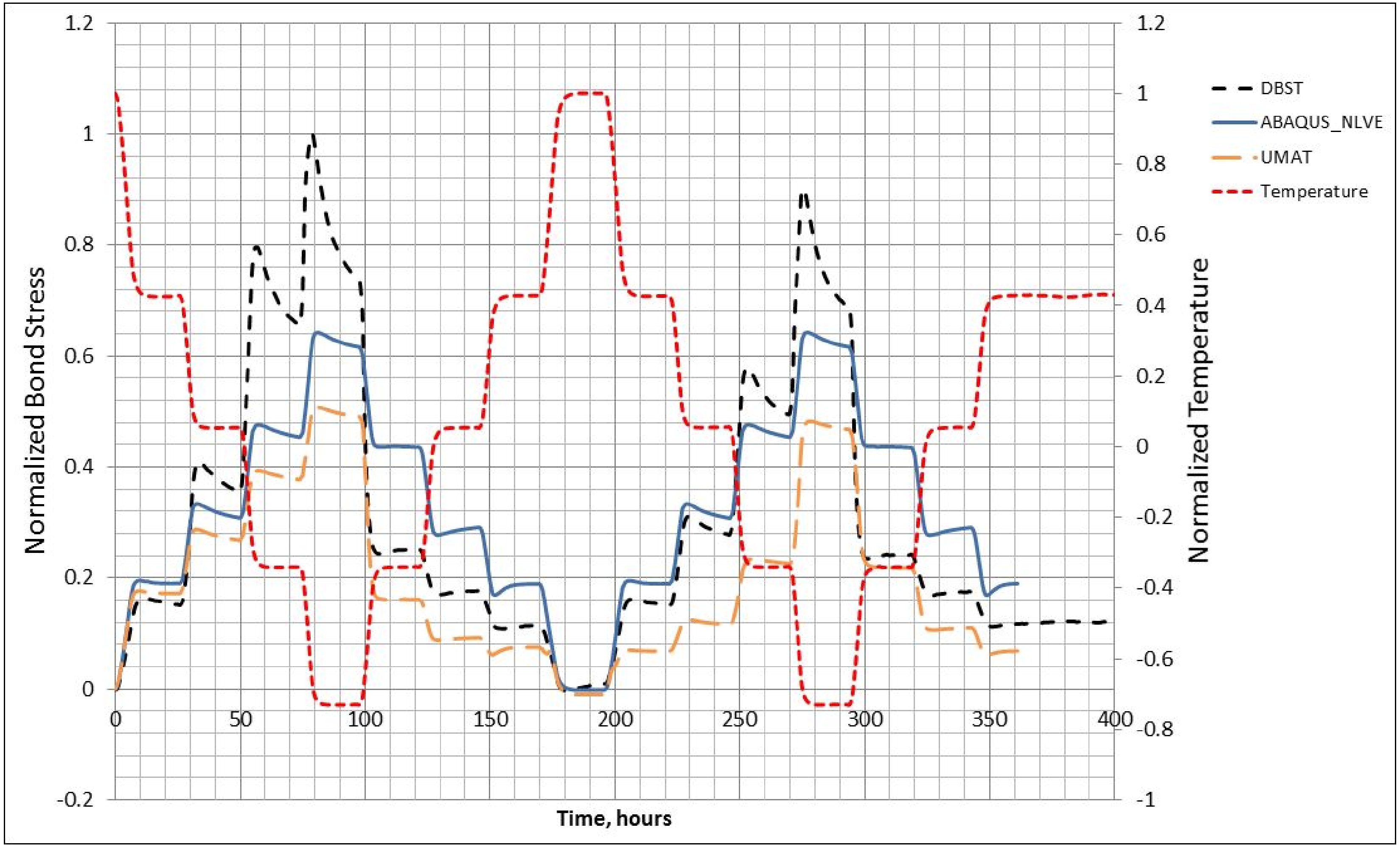

Figure 7.6. Bond stress and temperature history.

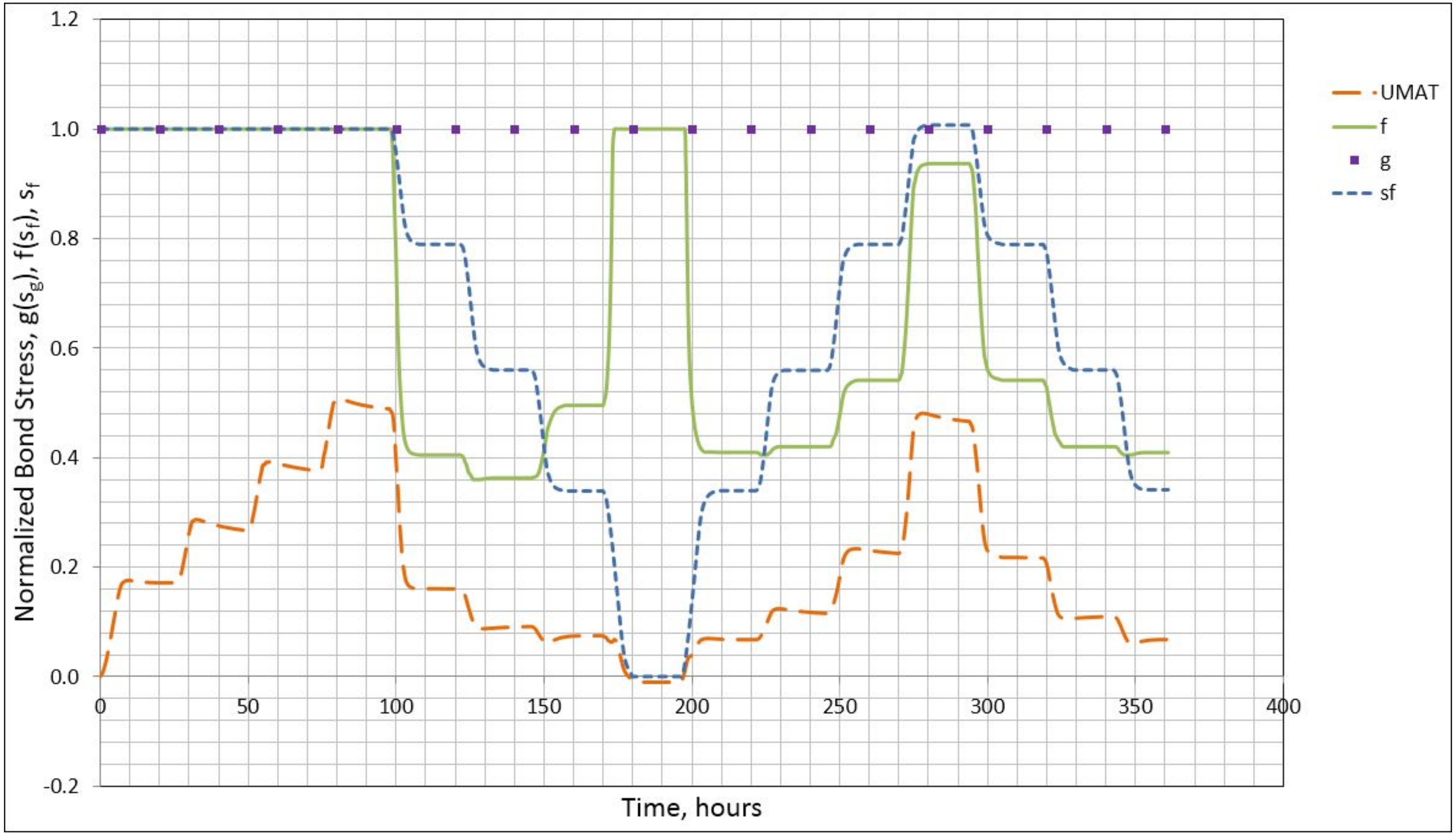

Figure 7.7. The history of cyclic softening function.

In order to further understand the difference in response between the built-in ABAQUS and the proposed model the evolution of the damage model parameters was investigated during cooling part of the loading history. State variables $c(t)$, $g(s_g)$, dilatation and bulk modulus normalized by its initial value, are shown in Figure 7.8. It is observed that $g(s_g)$ is equal to unity during the entire loading history. On the other hand the void content increases and as a consequence bulk modulus decreases during the first cooling. Therefore, even in the absence of $g(s_g)$, stress response softens due to softening of the bulk modulus.

In order to quantify the effect of the bulk modulus on the stress response, the stress response for constant bulk modulus was calculated. The predictions are shown in Figure 7.9. It is observed that the user material response is close to built-in ABAQUS model for first cooling. Afterwards the responses differ due to the effect of cyclic softening function $f(s_f)$.

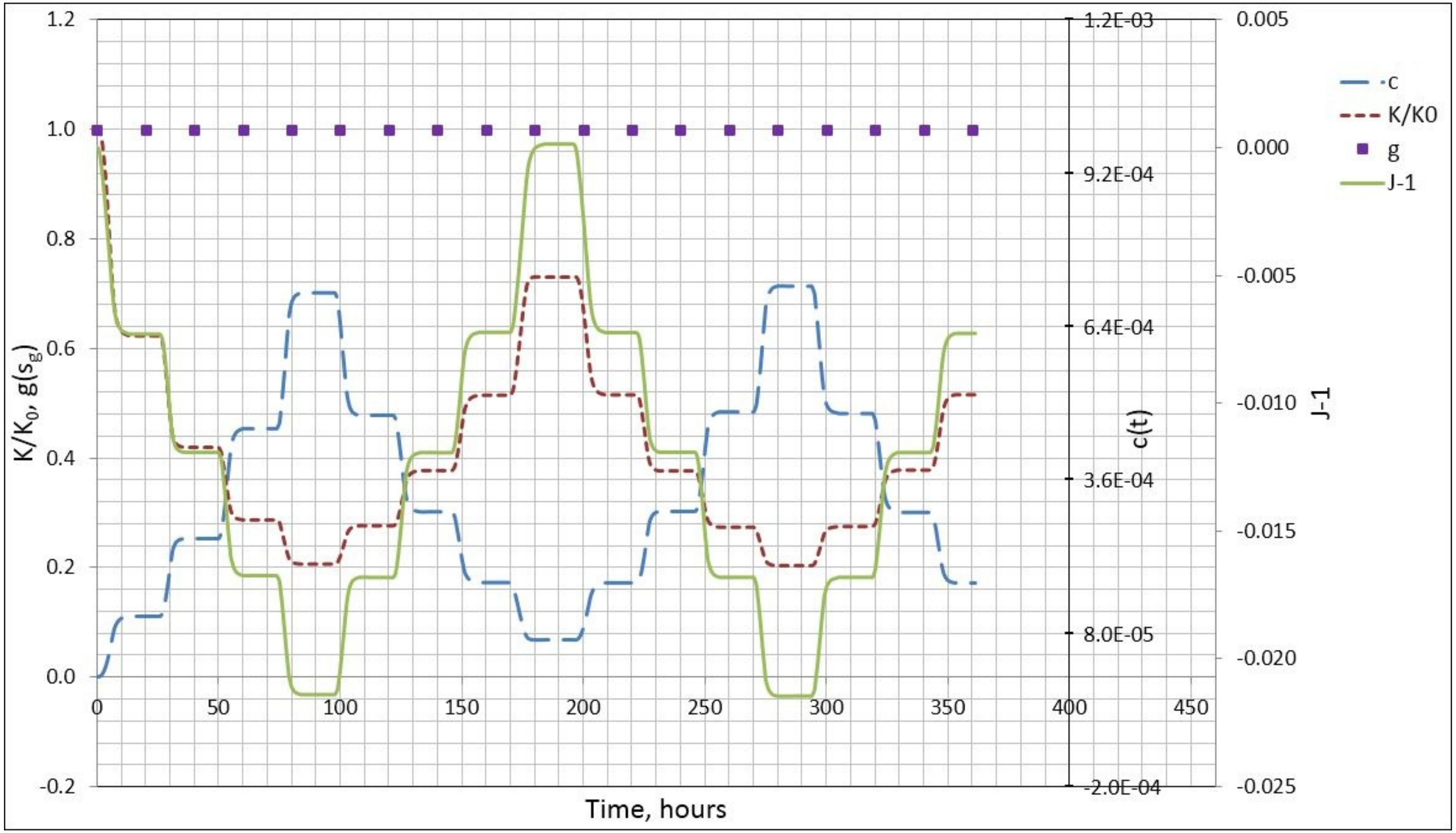

Figure 7.8. Evolution of state variables.

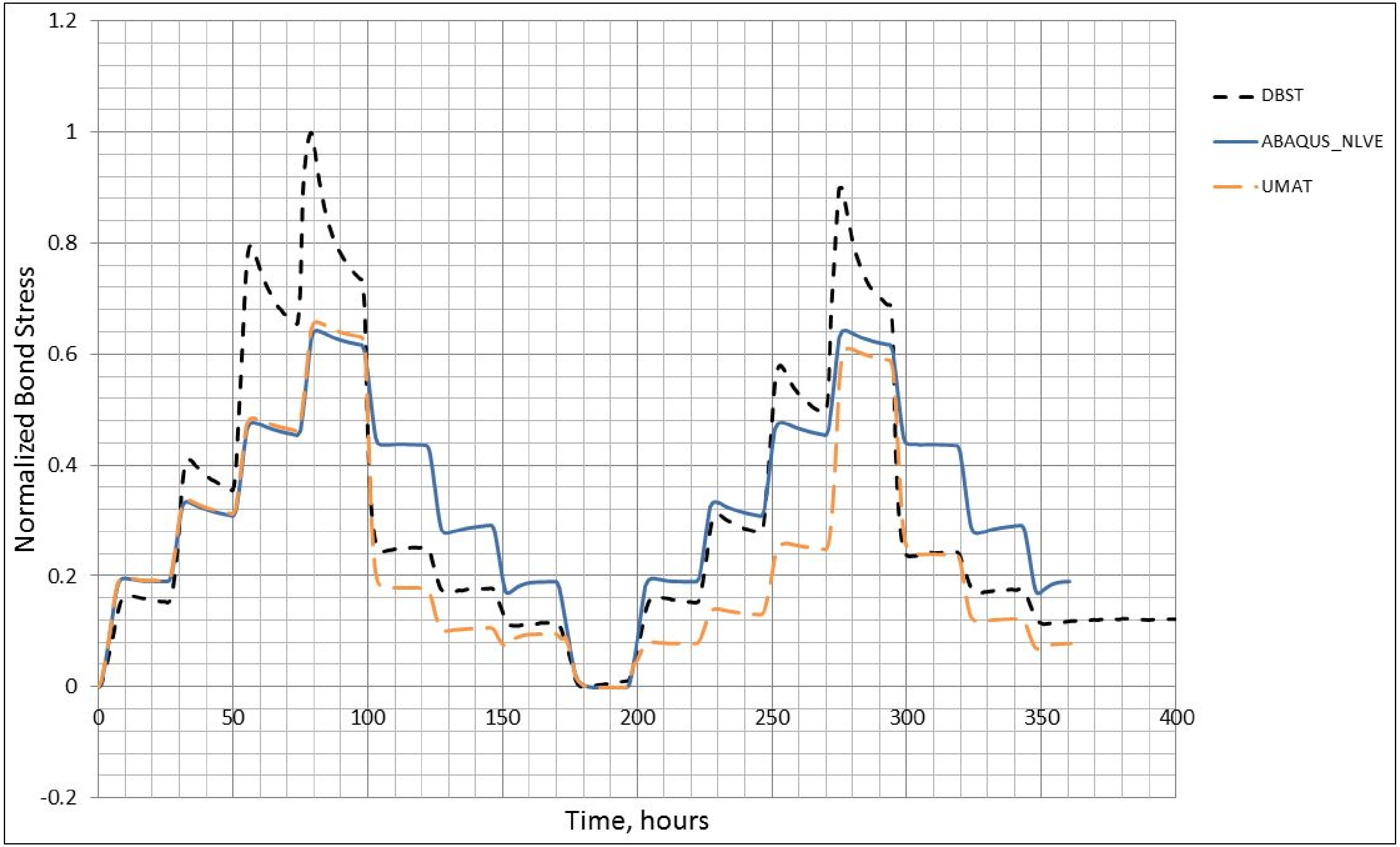

Figure 7.9. Bond stress predictions for $K(t) = K_0$.

In order to investigate the difference in predicted stress response and DBST measurements shown in Figure 7.6, the history of the calculated hoop strain is plotted as seen in Figure 7.10. It is noted that the hoop strain is quite low in that it is in the undamaged region of the material response. Furthermore the strain rate is much lower compared to the rate at which the constitutive model was calibrated. Thus, the underprediction in the cyclic thermal loading may be due to the fact that the material model underpredicted the response at low strain rates of uniaxial loading, as was shown in Figure 6.2. At this point, it is important to note that DBST stress data were not confirmed with alternative measurement techniques. Therefore, the accuracy of the sensor data may also play a role in disagreement between predictions and measurements.

In order to compensate for the strain rate effect Neo-Hookean coefficient c_{10} was calibrated to data for uniaxial constant strain rate loading at 0.00724 min^{-1}, which was the slowest available test. The rest of the model parameters were kept the same. The bond stress corresponding to this calibration is shown in Figure 7.11. The predicted maximum stress throughout the loading is still lower then the test data since the strain rate during thermal loading is much lower than 0.00724 min^{-1}.

As a summary, the proposed model and developed computational algorithm allowed to perform three dimensional finite element analysis of rocket motor under cyclic temperature loading. The softening of the stress response after first cycle was accounted for as a consequence of the softening function $f(s_f)$. The stress analysis of rocket motor that accounted for damage and unloading-reloading softening under cyclic temperature loading was not previously published in the literature.

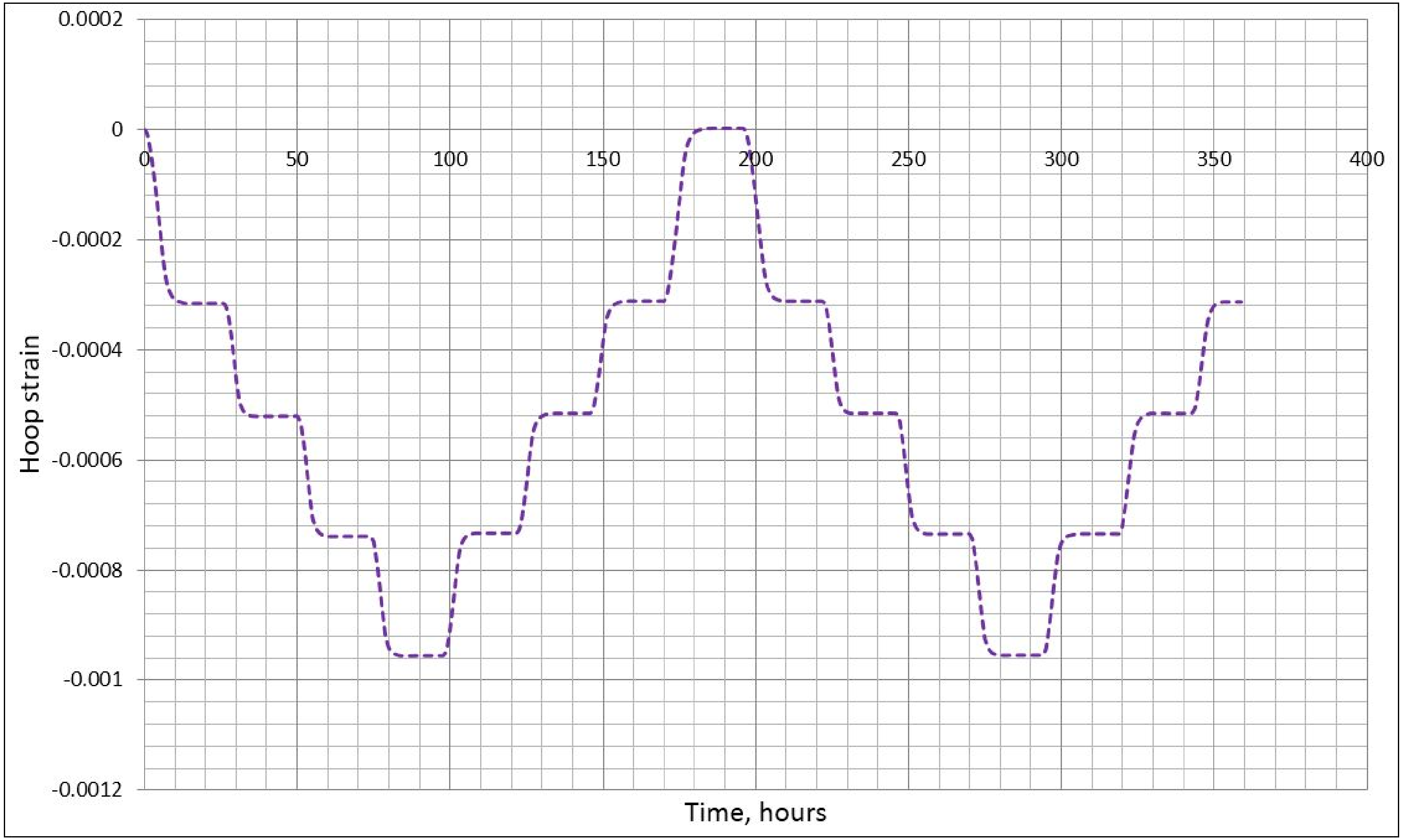

Figure 7.10. Hoop strain history.

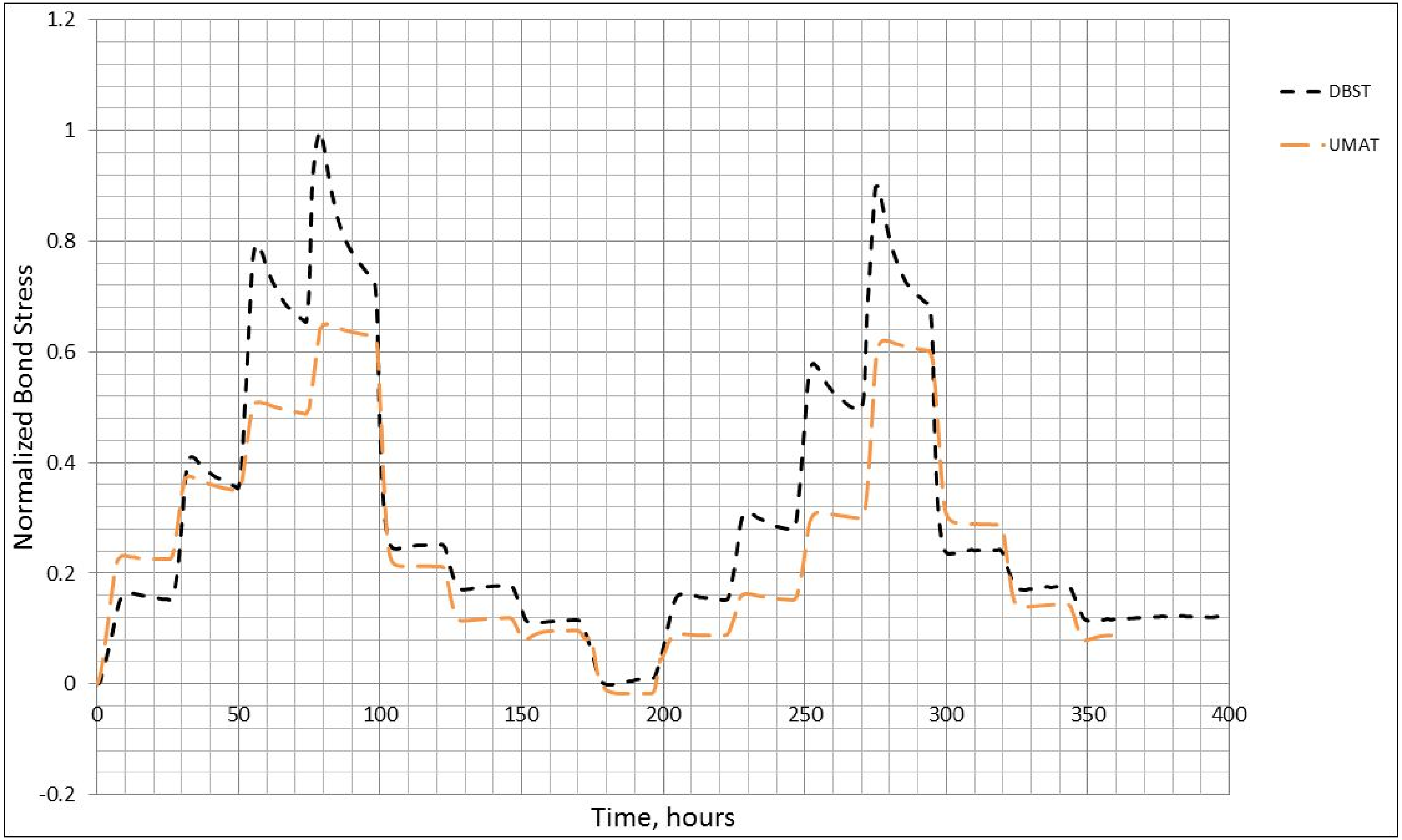

Figure 7.11. Bond stress history for a model calibrated at 0.00724 min^{-1}.

8. CONCLUSIONS

A summary of the work done in the dissertation is provided in this section. Based on the observations and the results obtained throughout the study, future recommendations regarding the areas that can be improved are discussed.

8.1. Summary and Contributions

A modified and enhanced version of a nonlinear viscoelastic constitutive model for solid propellants was proposed. The model accounts for the effects of strain rate, temperature, superimposed pressure, cyclic loading and interface debonding on the stress and dilatational response of the propellant. New criteria for damage initiation and evolution were presented. Cyclic function that accounts for the softening during unloading-reloading was used in a multiplicative form to viscoelastic stress in order to improve convergence during transition from unloading to loading.

Calibration of the constitutive model was explained and the set of equations to be used in calibration process were presented. Only two sets of test data were used for calibration.

Computational algorithm for the proposed model was developed and implemented into the commercial finite element software ABAQUS. The model with no damage was verified against the built-in material model available in the software using various types of solid elements. The damaging model was validated by comparing the results to the test data for various mechanical loads and thermal conditions. For verification and validation, one element model undergoing uniform deformations as well as multi element model with complex deformations were analysed. The implementation gave good results with respect to the built-in model in ABAQUS and the test data for uniform as well as non-uniform loading and boundary conditions.

A finite element model of a rocket motor composed of steel casing and propellant grain was prepared and three dimensional stress analysis was performed under cyclic temperature loading representing storage conditions.

It was concluded that the developed numerical algorithm is robust in terms of computational performance and convergence behaviour.

Main outcome of this dissertation is the developed computational procedure that employs a constitutive model that accurately represents the essential mechanical characteristics of the grain, and that allows to perform three dimensional finite element analysis of a solid rocket motor exposed to general environmental conditions and loads. The model and the algorithm can also be used for other elastomeric materials. The implementation of the constitutive model allows to investigate the effect of various forms of damage models on the stress response of elastomeric materials during three dimensional stress analysis.

8.2. Discussion and Recommendations

According to the results presented in this dissertation, an important area for the future work is the improvement of the predictive capability of the model at various rates. The results showed that the response is underpredicted at strain rates lower than the rate at which the model was calibrated and overpredicted at strain rates higher than the calibration rate. This phenomenon is observed at strains where stress softening is negligible. Thus, modelling of viscoelasticity through the convolution integral may not be valid for solid propellants.

The overprediction of the stress relaxation response at low temperatures may be a consequence of using WLF function to represent the shift function in the constitutive model. Alternative approach would be to construct tables containing the values of shift function at various temperatures and interpolate the necessary value from those tables. The effect of variation of the shift function for different loading conditions can be investigated in more detail.

Another area of future work is the predictive capability of the model at multiple cyclic loadings. The test data for uniaxial cyclic load shows that the peak value of stress decreases at each cycle. The current constitutive model accounts for decrease of stress at the end of first cycle only. Fatigue simulation may be combined with the constitutive model.

The future work regarding the computational algorithm might be the use of other forms of strain energy density functions. Although Neo-Hookean strain energy density function is used in this dissertation, computational algorithm is provided in a general form so that it allows straightforward implementation of other forms of strain energy functions. The performance of Yeoh or Mooney-Rivlin polynomials can be investigated in terms of predictive capability of the model and numerical performance of the computational algorithm.

The computational algorithm in this dissertation is provided for both non-damaging and damaging constitutive models. Implementation of the damage model into the computational algorithm is clearly presented. The procedure followed for the numerical integration of evolution equations of damage model was explained in detail. Although the damage model provided in this dissertation was developed to represent dewetting, models simulating other damage mechanisms for solid propellants, as well as other highly filled elastomers, can easily be implemented into the algorithm. That is, the model and its numerical algorithm are general enough to be used for the three dimensional stress analysis of viscoelastic materials other than solid propellants.

The model and its implementation may be readily used for the stress analysis of hyperelastic materials such as rubber by omitting viscoelastic effects. This can be done in two ways. The first one is to set the coefficients of the Prony series to zero and replace the long term moduli by the instantaneous moduli. This method does not require any modifications of the algorithm. The second way is to use the elastic form of second Piola-Kirchhoff stress presented in the dissertation and derive the tangent stiffness accordingly. This can be achieved with minor modifications in the algorithm.

Another important area regarding the performance of the computational algorithm is the rate of convergence of the model under various types of finite element analysis. The number of increments and the time for converged solution should be compared to those of built-in ABAQUS model. In order to obtain faster solution, an alternative approach might be provided. The tangent stiffness with respect to Cauchy stress can be derived. This approach eliminates the necessity of using transformation equations to convert tangent stiffness of second Piola-Kirchhoff stress to the Eulerian form which results in many computations at each integration point.

In this dissertation, the computational algorithm was developed for implicit simulations which needs the definition of tangent stiffness. Alternatively, a computational algorithm for the explicit simulations can be developed, so that, transient simulations, impact loading, in flight loading can also be performed.

In addition to the recommendations above, the extent of service life of the rocket motor can be investigated based on the results obtained from the three dimensional stress analysis. The most straightforward method would be to use the standard approaches in the literature and determine failure based on various stress analyses. Alternatively new methodologies can be developed by combining constitutive and failure theories.

REFERENCES

1. *ABAQUS User's Manual*, Dassault Systems Simulia Corp., 2012, version 6.12.

2. Simo, J. C., "On a fully three-dimensional finite-strain viscoelastic damage model: formulation and computational aspects.", *Computer Methods in Applied Mechanics and Engineering*, Vol. 60, pp. 153–173, 1987.

3. Park, S. and R. Schapery, "A viscoelastic constitutive model for particulate composites with growing damage.", *International Journal of Solids and Structures*, Vol. 34, pp. 931–947, 1997.

4. Jinsheng, X., C. Xiong, W. Hongli, Z. Jian and Z. Changsheng, "Thermo-damage-viscoelastic constitutive model of HTPB composite propellant.", *International Journal of Solids and Structures*, Vol. 51, pp. 3209–3217, 2014.

5. Ha, K. and R. Schapery, "A three-dimensional viscoelastic constitutive model for particulate composites with growing damage and its experimental validation.", *International Journal of Solids and Structures*, Vol. 34, pp. 3497–3517, 1998.

6. Wang, Z., H. Qiang, G. Wang and Q. Huang, "Tensile mechanical properties and constitutive model for HTPB propellant at low temperature and high strain.", *Journal of Applied Polymer Science*, 2015.

7. Xu, F., P. Sofronis, N. Aravas and S. Meyer, "Constitutive modeling of porous viscoelastic materials.", *European Journal of Mechanics A/Solids*, Vol. 26, pp. 936–955, 2007.

8. Han, L., X. Chen, J.-S. Xu, C.-S. Zhou and J.-Q. Yu, "Research on the time-temperature-damage superposition principle of NEPE propellant.", *Mechanics of Time-Dependent Materials*, Vol. 19, pp. 581–599, 2015.

9. Deng, B., Y. Xie and G. J. Tang, “Three-dimensional structural analysis approach for aging composite solid propellant grains.”, *Propellants, Explosives, Pyrotechics*, Vol. 39, pp. 117–124, 2014.

10. Jung, G.-D. and S.-K. Youn, “A nonlinear viscoelastic constitutive model of solid propellant.”, *International Journal of Solids and Structures*, Vol. 36, pp. 3755–3777, 1999.

11. Vratsanos, L. and R. Farris, “A predictive model for the mechanical behaviour of particulate composites. Part 1: Model derivation, Part 2: Comparison of model predictions to literature data.”, *Polymer Engineering and Science*, Vol. 33, pp. 1458–1474, 1993.

12. Jung, G.-D., S.-K. Youn and B.-K. Kim, “A three-dimensional nonlinear viscoelastic constitutive model of solid propellant.”, *International Journal of Solids and Structures*, Vol. 37, pp. 4715–4732, 2000.

13. Yun, K.-S., J. Park, G.-D. Jung and S.-K. Youn, “Viscoelastic constitutive modeling of solid propellant with damage.”, *International Journal of Solids and Structures*, Vol. 80, pp. 118–127, 2016.

14. Chyuan, S.-W., “A study of a loading history effect for thermoviscoelastic solid propellant grains.”, *Computers and Structures*, Vol. 77, pp. 735–745, 2000.

15. Chyuan, S.-W., “Nonlinear thermoviscoelastic analysis of solid propellant grains subjected to temperature loading.”, *Finite Elements in Analysis and Design*, Vol. 38, pp. 613–630, 2002.

16. Hur, J., J.-B. Park, G.-D. Jung and S.-K. Youn, “Enhancements on a micromechanical constitutive model of solid propellant.”, *International Journal of Solids and Structures*, Vol. 87, pp. 110–119, 2016.

17. Huiru, C., T. Guojin and S. Zhibin, “A three-dimensional viscoelastic constitutive

model of solid propellant considering viscoelastic Poisson's ration and its implementation.", *European Journal of Mechanics A/Solids*, Vol. 61, pp. 235–244, 2017.

18. Guo, X., J.-T. Zhang, M. Zhang, L.-S. Liu, P.-C. Zhai and Q.-J. Zhang, "Effect of liner properties on the stress and strain along liner/propellant interface in solid rocket motor.", *Aerospace Science and Technology*, Vol. 58, pp. 594–600, 2016.

19. Liu, C. and D. Thompson, "Mechanical response and failure of high performance propellant (HPP) subject to uniaxial tension.", *Mechanics of Time-Dependent Materials*, Vol. 19, pp. 95–115, 2015.

20. Liu, C.-W., J.-H. Yang, X.-M. Wang and Y.-K. Ma, "The damage low of HTPB propellant under thermo mechanical loading.", *Journal of Energetic Materials*, Vol. 34:1, pp. 1–13, 2016.

21. Bin, D., S. Zhibin, D. Jingbo and T. Guojin, "Finite element method for viscoelastic medium with damage and the application to structural analysis of solid rocket motor grain.", *Science China - Physics, Mechanics and Astronomy*, Vol. 57, pp. 908–915, 2014.

22. Ozupek, S. and E. Becker, "Constitutive equations for solid propellants.", *Journal of Engineering Materials and Technology*, Vol. 199, pp. 125–132, 1997.

23. Canga, M., E. Becker and Ş. Özüpek, "Constitutive modelling of viscoelastic materials with damage – computational aspects.", *Computer Methods in Applied Mechanics and Engineering*, Vol. 190, pp. 2207–2226, 2001.

24. Little, R., H. Chellner and H. Buswell, "Development, Testing and Application of Embedded Sensors for Solid Rocket Motor Health Monitoring.", *37th International Annual Conference of ICT, Frauenhofer Institut Fur Chemische Technologie*, pp. 21–1, 2006.

25. Hughes, T. J. R., *The Finite Element Method, Linear Static and Dynamic Finite*

Element Analysis, John Wiley & Sons, Inc., New York, NY, USA, 2000.

26. Crisfield, M., *Non-linear Finite Element Analysis of Solids and Structures*, John Wiley & Sons, Inc., New York, NY, USA, 2000.

27. Zienkiewicz, O., R. Taylor and J. Z. Zhu, *The Finite Element Method Its Basis & Fundamentals*, Elsevier, Great Britain, 2005.

28. Zienkiewicz, O. and R. Taylor, *The Finite Element Method for Solid and Structural Mechanics*, Elsevier, Great Britain, 2005.

29. Ogden, R., *Nonlinear Elastic Deformations*, John Wiley & Sons, Inc., New York, NY, USA, 1997.

30. Reddy, J. N., *An Introduction to Continuum Mechanics*, Cambridge University Press, New York, NY, USA, 2008.

31. Reddy, J. N., *An Introduction to the Finite Element Method*, McGraw-Hill, New York, NY, USA, 2006.

32. Chapra, S. C. and R. P. Canale, *Numerical Methods for Engineers*, McGraw-Hill, New York, NY, USA, 2006.

33. Mase, G. T. and G. E. Mase, *Continuum Mechanics for Engineers*, CRC Press, Florida, USA, 1999.